Supporting Information

Delaminated MBene Sheets Beyond Usual 2D Transition Metal Materials for Securing Pt Single Atoms to Boost Hydrogen Evolution

Seok Ju Park[a], Thanh Hai Nguyen[a], Duy Thanh Tran[a], Van An Dinh[b], Nam Hoon Kim[a], Joong Hee Lee[a,c]*

[a]Department of Nano Convergence Engineering, Jeonbuk National University, Jeonju, Jeonbuk, 54896, Republic of Korea.

[b]Department of Precision Engineering, Graduate School of Engineering, Osaka University, 2-1, Yamada-oka, Suita, Osaka 565-0871, Japan.

[c]Carbon Composite Research Center, Department of Polymer-Nano Science and Technology, Jeonbuk National University, Jeonju, Jeonbuk, 54896, Republic of Korea.

Chemical materials

All the chemicals and reagents were commercially available and used directly without further purification. MoAlB phase powder (400 mesh) was purchased from Laizhou Kai Kai Ceramic Materials Co., Ltd (China). Sulfuric acid (H_2SO_4, 95%), potassium hexachloroplatinate (K_2PtCl_6, 99%), L-Ascorbic acid ($C_6H_8O_6$, 99%), tetramethylammonium hydroxide (TMAOH) ($(CH_3)_4N(OH)$, 25wt% in H_2O), and molybdenum carbide powder (Mo_2C, 325 mesh, 99.5%) were obtained from Sigma-Aldrich. Sodium hydroxide (NaOH, 98%), potassium hydroxide (KOH, 85%), and 2-Propanol (C_3H_7OH, 99.9%) were provided from Samchun Chemical Co. (Korea). Nanocrystalline powder of molybdenum (IV) sulfide sheet (MoS_2, 325 mesh, 99 %) was provided from Alfa Aesar Co. (USA).

Structural characterization

The field-emission scanning electron microscopy (FE-SEM) on a GeminiSEM 500 instrument (Zeiss, Germany) and transmission electron microscopy (TEM) on a JEM-ARM200F instrument (JEOL Ltd., Japan) were used to probe morphology and micro/nano/atomic-scale structure of the synthesized materials. The valance state and chemical composition were investigated by conducting X-ray photoelectron spectroscopy (XPS) on a Theta Probe instrument (Thermo Fisher Scientific Inc., USA) at the KBSI center, Jeonju. Specific surface area and porosity of the synthesized materials were measured by using an ASAP 2020 Plus system (Micromeritics Instrument Co., USA). Crystalline features of the synthesized materials were investigated by X-ray diffraction (XRD) via a D/Max 2500 V/Pc instrument (Rigaku Co., Japan). Chemical properties of the synthesized materials were examined by a micro-Raman spectrum of RAMANtouchlaser analysis system with excitation λ= 532 nm (Nanophoton Co., Japan) and XAS analysis on a Rigaku R-XAS instrument (Rigaku Co. Japan) with an accelerated voltage/Current of 10 kV/50 mA. The metal content of the synthesized materials was assessed by analytical technique of inductively coupled plasma-optical emission spectroscopy (ICP-OES) via an iCAP 7400 Duo instrument (Thermo Fisher Scientific Co., USA).

Electrochemical measurement

All electrochemical measurements were studied in a three-electrode electrochemical cell integrated with a CHI660D system manufactured by CH Instruments Inc. (USA). A graphite rod and Ag/AgCl (saturated KCl) were employed as counter and reference electrodes, respectively. The catalyst ink-coated Ni foam (NF) or carbon cloth (CC) was utilized as the working electrode in a 1.0 M KOH or 0.5 M H_2SO_4 electrolyte. For preparing the working electrodes, a homogeneous catalyst ink was made by ultrasonication a mixture of active material (2.5 mg), carbon black (0.5 mg), IPA (750 μL), and Nafion 5wt% (25 μL) for 60 min.

The ink was then drop-casted on NF or CC, followed by naturally drying overnight. The catalytic activity of electrodes was measured by linear sweep voltammetry (LSV) taken at a slow scan rate of 5 mV s^{-1} to minimize the capacitive contribution. The hetero charge transfer capability of electrode was measured by electrochemical impedance spectroscopy (EIS) in a frequency range from 10^5 to 10^{-2} Hz at open circuit potential (OCP), shown in Table S1. For comparison, the electrodes of commercial Pt-C were also prepared in the same approach. All the measured potentials were converted to reversible hydrogen electrode by using the following equation.

$$E_{RHE} = E_{Ag/AgCl} + E^{0}_{Ag/AgCl} + 0.0592 \times pH \qquad (1)$$

Fabrication of anion exchange membrane water electrolyzer (AEMWE) single-cell and characterization

The AEMWE single cell was constructed with an active area of 5 cm^2. The Sustainion Anion Exchange Membrane (X37−50, Grade T) was used to separate the anode and cathode components, and they were immersed in a bath of 1.0 M KOH for 48 h to exchange chloride ions to hydroxide ions fully. The anode catalyst ink was prepared by mixing 40 mg of RuO_2 with 1.5 g of IPA:H_2O (3:1, w/w) and 300 μL of Sustainion® XA−9 Alkaline Ionomer 5% in EtOH. The cathode catalyst ink was prepared by mixing 15 mg of Pt–$MoAl_{1-x}B$ with 5 mg of carbon black (CAS No: 133-86-4, Korea Carbon Black Co., Ltd), 1.5 g of IPA:H_2O (3:1, w/w), and 300 μL of Sustainion® XA−9 Alkaline Ionomer 5% in EtOH. The anode and cathode inks were sonicated for 1.0 h in an iced bath and spray−coated on stainless-steel fiber paper (anode) and carbon cloth (cathode), respectively, using a hand-spray method with the assistance of air−spray gun. Afterward, the electrodes were moved to a vacuum oven for drying at 60 °C overnight. The catalyst loading was 5.0 and 3.0 mg cm^{-2} at anode and cathode electrodes,

respectively. The *I–V* curves of the AEMWE cell were recorded in 1.0 M KOH at 60 °C by scanning current at a step rate of 5 mA using an in-house-produced water electrolyzer (Carbon and Fuelcell, Korea). The AEMWE cell durability was evaluated at a constant current density of 0.5 A cm^{-2} at 60 °C. The electrolyte was circulated at a rate of 3 mL min^{-1} through a peristaltic pump. The cell efficiency (%) of the AEMWE cell is calculated as follows:[1,2]

$$Cell\ efficiency\ (\%) = \frac{Hydrogen\ power}{AEMWE\ power} \times 100\% \quad (2)$$

Where hydrogen power ($\frac{W}{cm^2}$) = hydrogen production rate × lower heating value, and AEMWE power ($\frac{W}{cm^2}$) = cell voltage × cell current density. In this study, we assumed that the Faradic efficiency of hydrogen is 100 %, hence the hydrogen production rate is theoretically 2.59 × 10^{-6} mol H_2/(cm^2·s) at 0.5 A cm^{-2}. A lower heating value is 24 200 J/mol.

Density functional theory calculation

DFT studies were performed by using Vienna Ab initio Simulation Package (VASP) code.[3,4] The projector-augmented wave (PAW) method was employed to describe the interaction between electron and core.[5] The Perdew-Burke-Ernzerhof (PBE) functional within the generalized-gradient approximation (GGA) was utilized to describe the electron exchange correlation.[6] An energy cutoff of 500 eV was chosen for plane-wave basis set, and the Γ-centered k-point for all calculations was automatically generated by the value of 0.03 (unit of 2π $Å^{-1}$) by using VASPKIT.[7] The spin-polarization and Grimme's D3 scheme of vdW correction were considered in all calculations.[8] To avoid the self-interaction between their periodic images, a vacuum layer of 15 Å was added. During the structural relaxation, all atoms were freely moved until the convergence tolerance of force reached less than 0.02 eV $Å^{-1}$. The

free energy was calculated by:

$$\Delta G = \Delta E + \Delta ZPE - T\Delta S \quad (3)$$

where ΔE is the total energy difference. The ΔZPE and ΔS are the change in zero-point energy and entropy, respectively. T is the temperature (298.15 K).

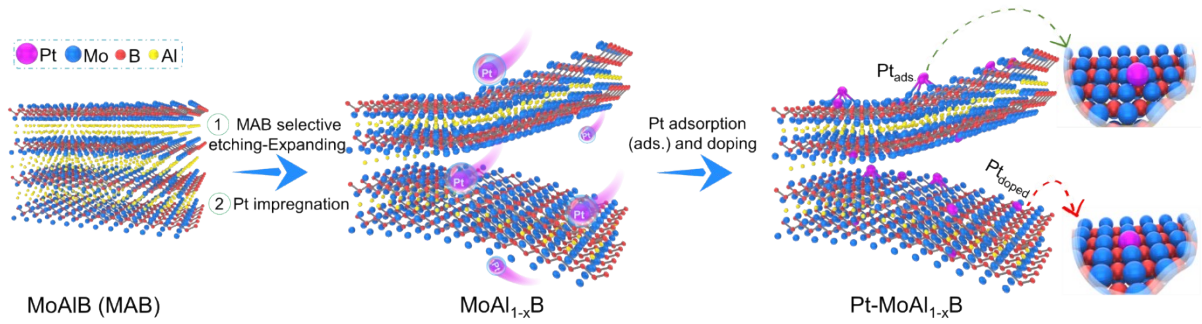

Figure S1. Schematic illustration for the fabrication of Pt–$MoAl_{1-x}B$ catalyst.

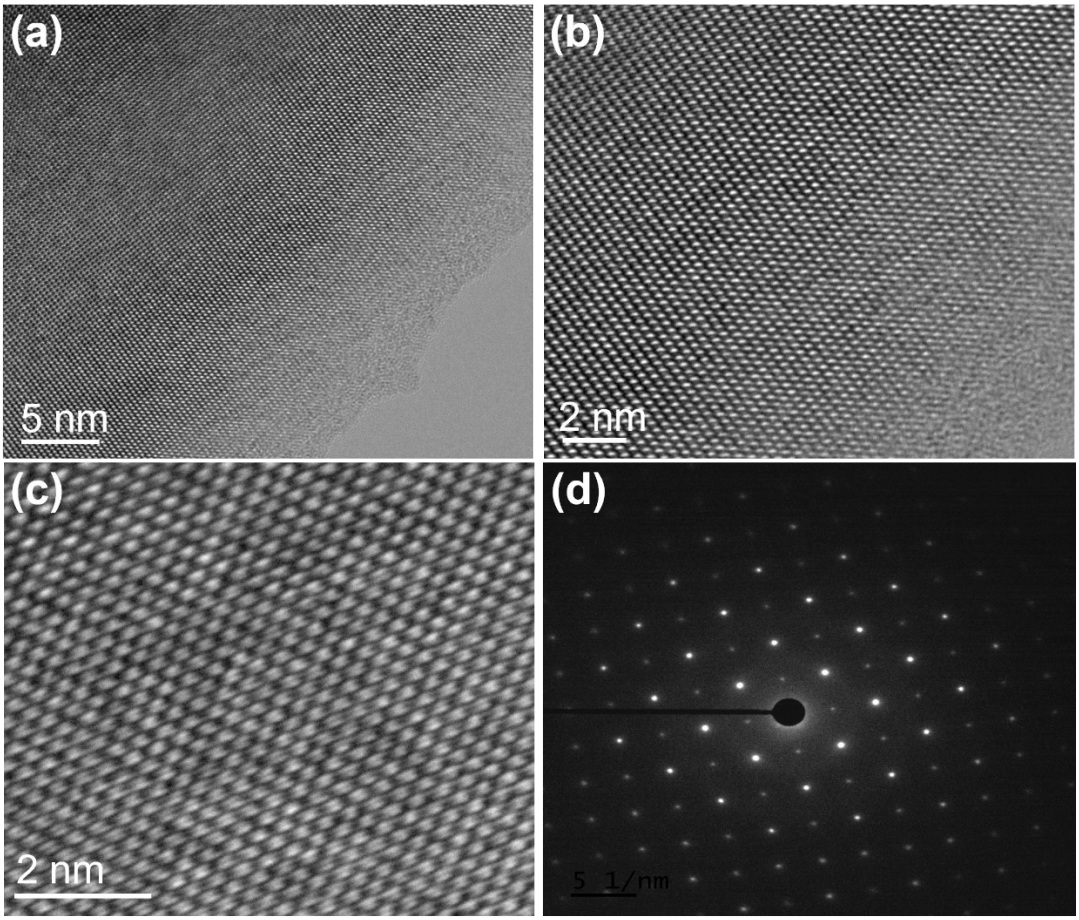

Figure S2. HR-TEM images and SAED spectrum of the MAB structure.

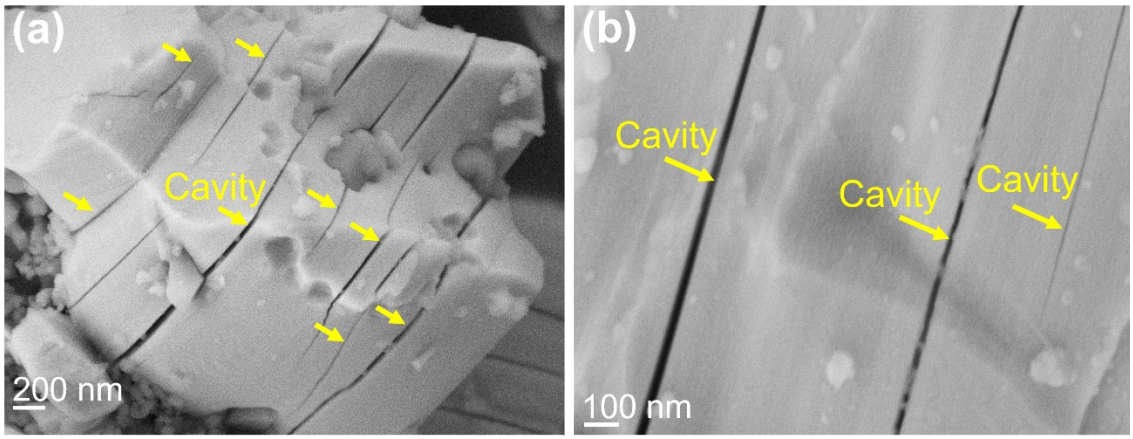

Figure S3. SEM image of MAB after alkaline treatment.

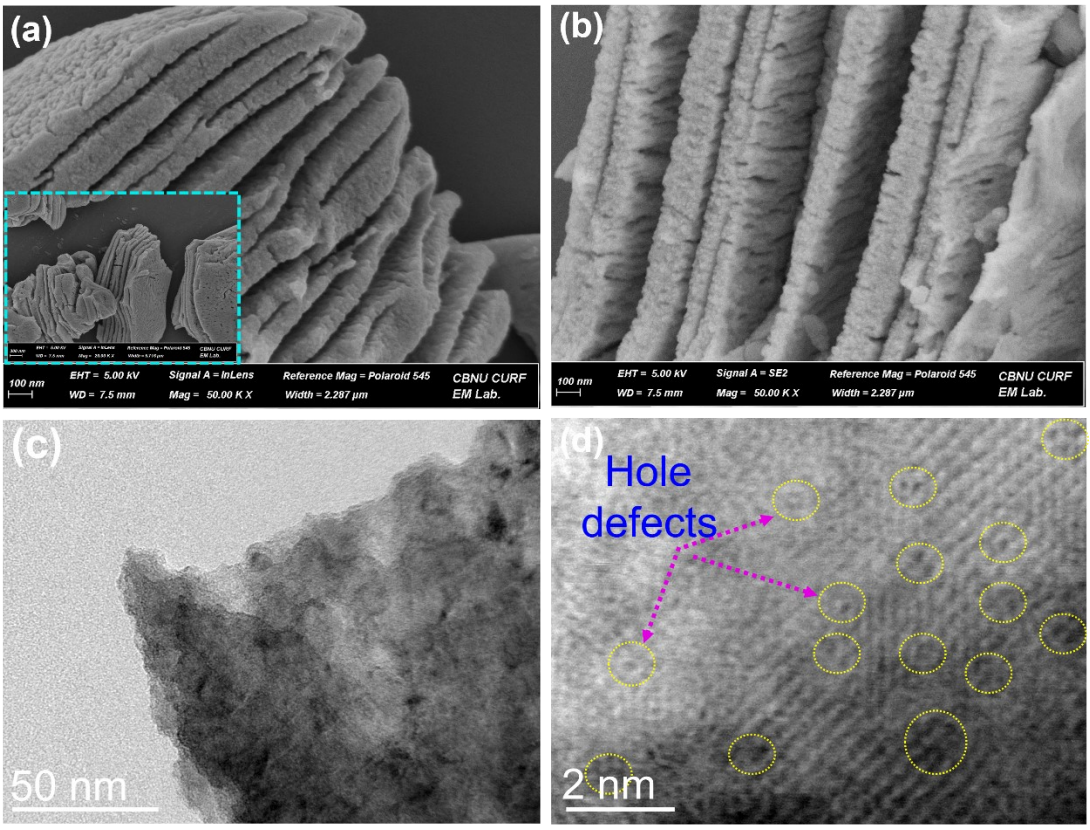

Figure S4. (a and b) SEM; (c) TEM and HR-TEM (d) images of $MoAl_{1-x}B$ material.

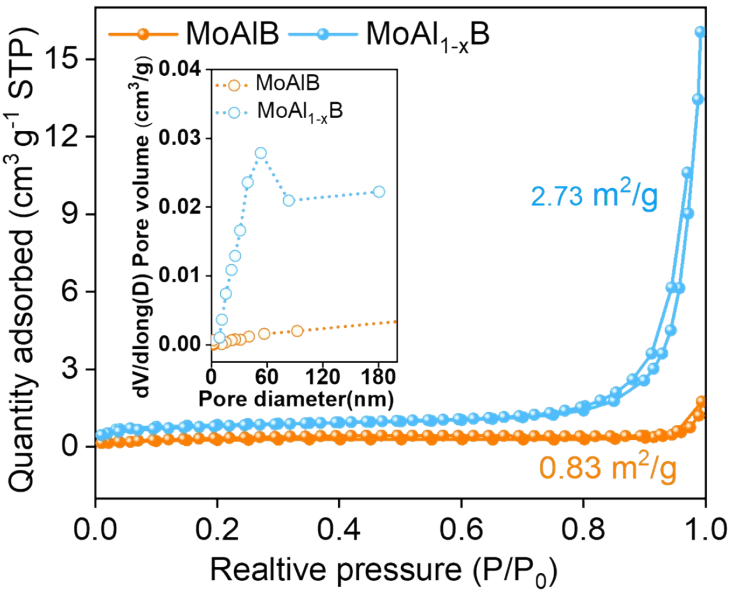

Figure S5. Nitrogen adsorption-desorption isotherms for bulk MAB and $MoAl_{1-x}B$ materials

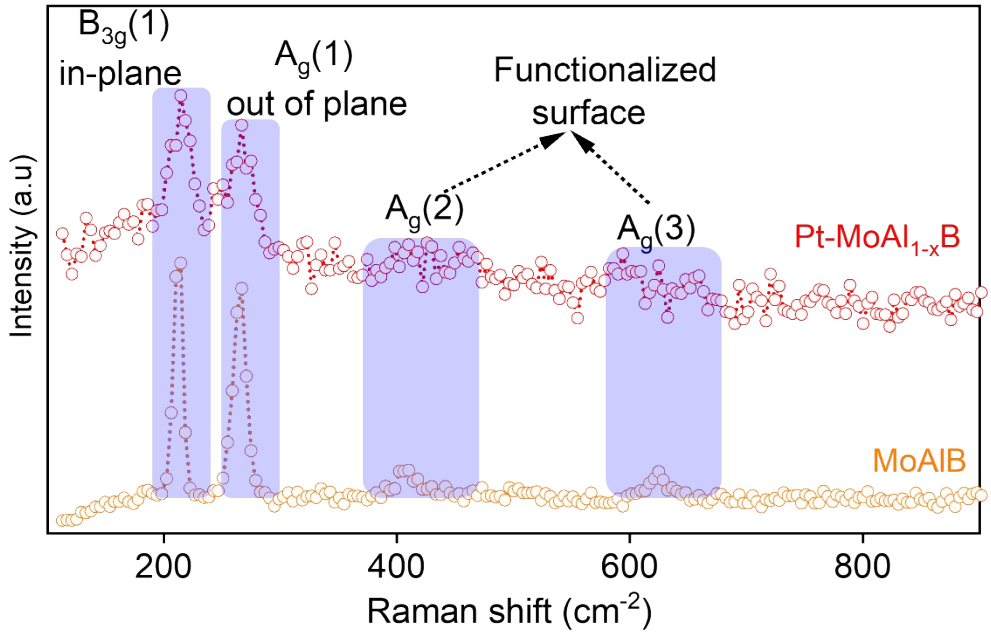

Figure S6. Raman spectra of the Pt–$MoAl_{1-x}B$ and MAlB materials.

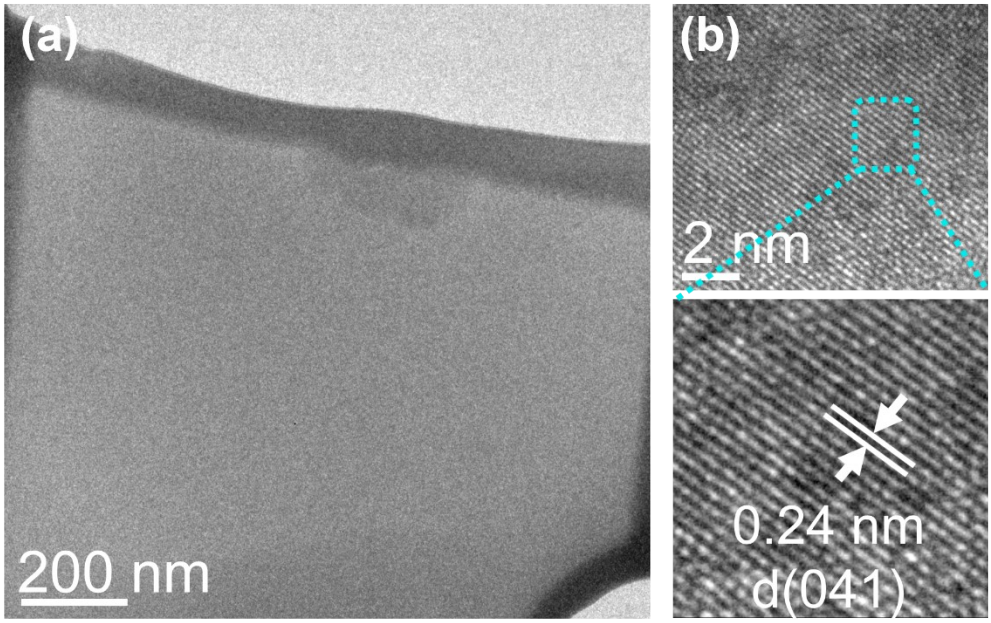

Figure S7. (a) TEM and (b) HR-TEM images of Pt–$MoAl_{1-x}B$ material.

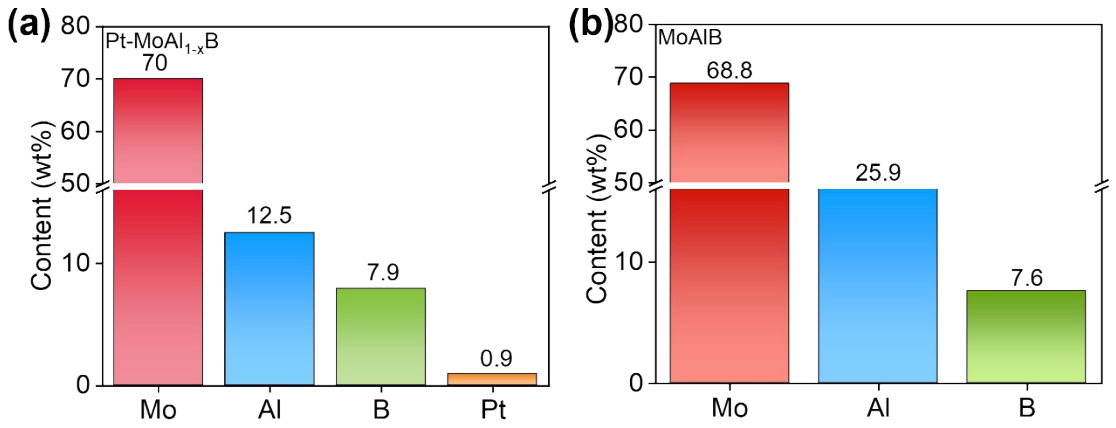

Figure S8. Element percentages of (a) Pt–$MoAl_{1-x}B$ and (b) MoAlB materials measured by ICP–OES.s

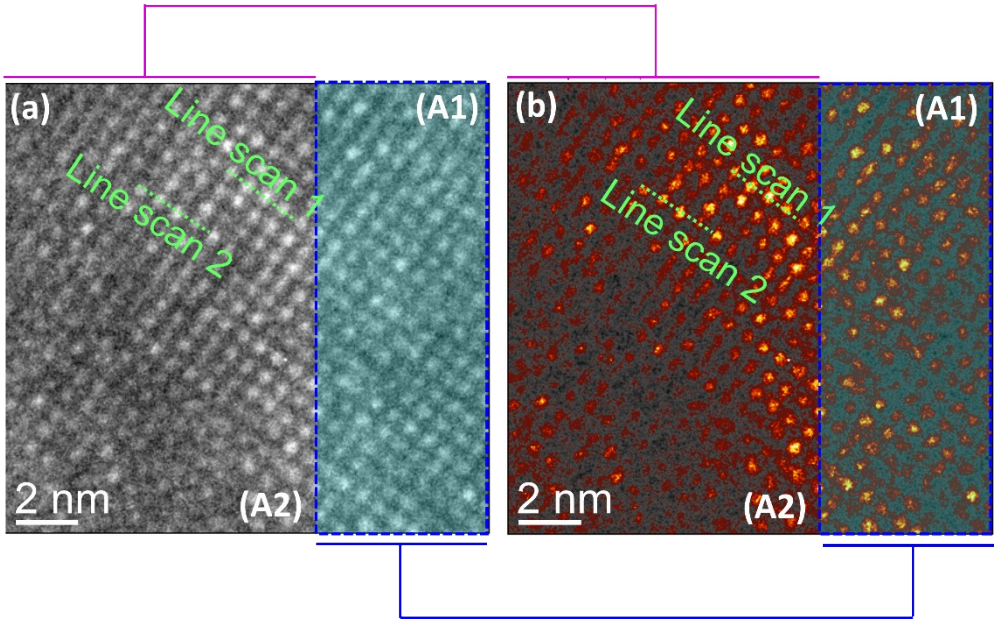

Figure S9. (a) HAADF–STEM image of Pt–$MoAl_{1-x}B$ material and (b) its corresponding false-color image.

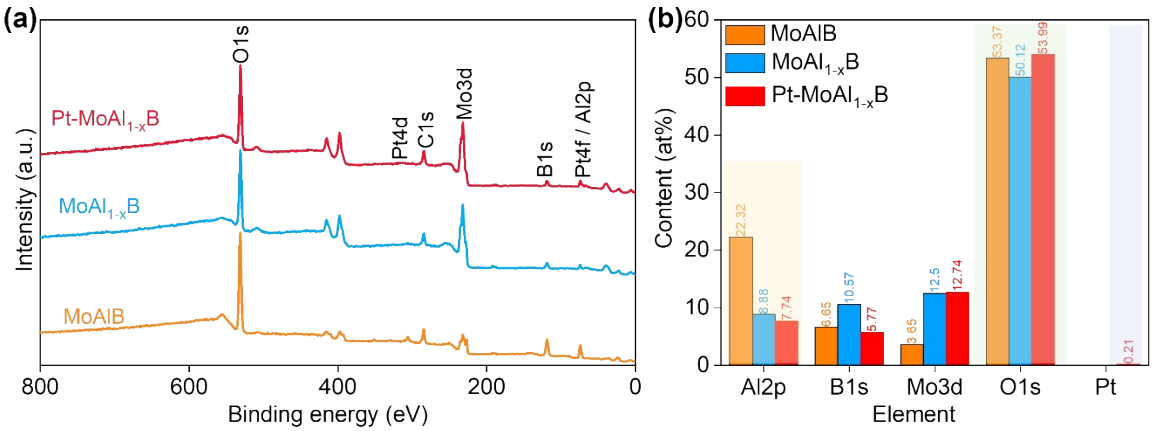

Figure S10. (a) XPS survey of Pt–$MoAl_{1-x}B$, $MoAl_{1-x}B$, and MoAlB materials; (b) Atomic percentage of Al2p, B1s, Mo3d, O1s, and Pt in Pt–$MoAl_{1-x}B$, $MoAl_{1-x}B$, and MoAlB materials.

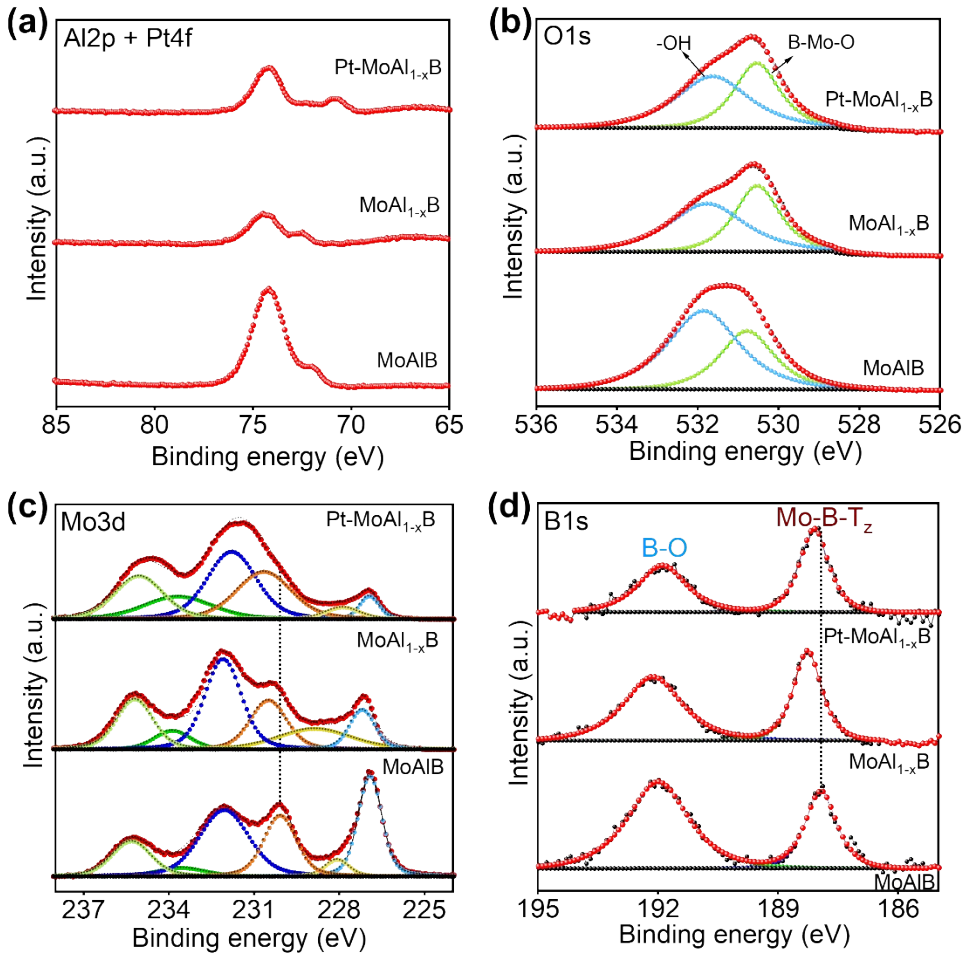

Figure S11. High resolution XPS spectra of (a) Al2p + Pt4f, (b) O1s, (c) Mo3d and (d) B1s in Pt–$MoAl_{1-x}B$, $MoAl_{1-x}B$, and MoAlB materials

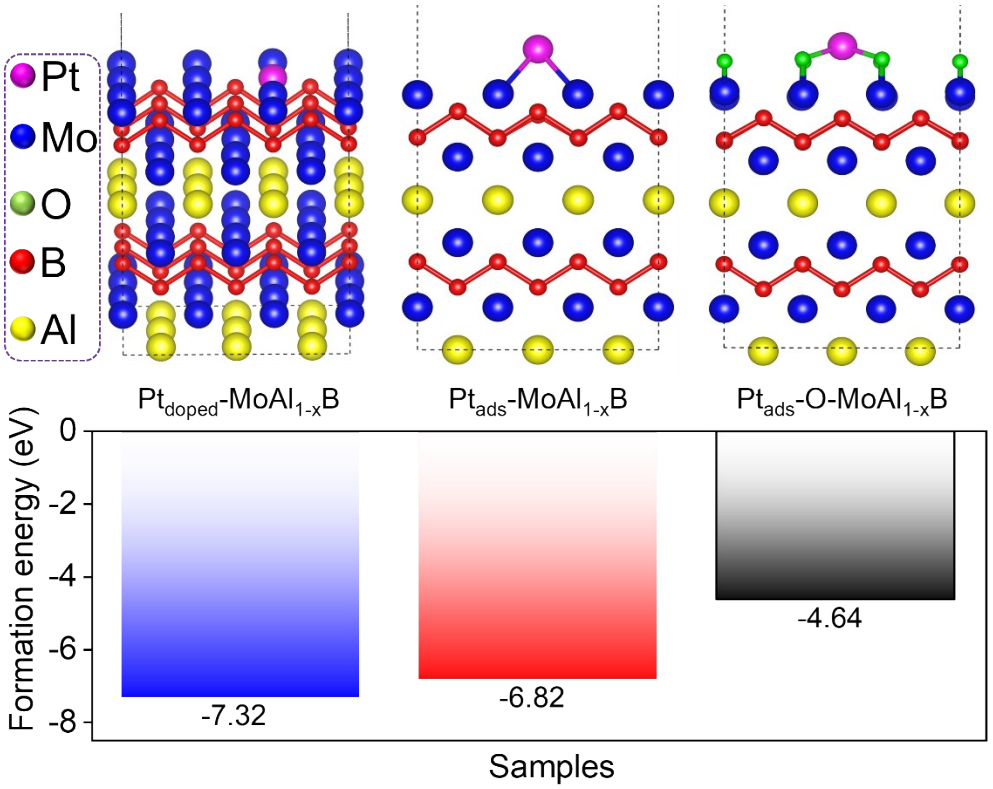

Figure S12. The formation energy for Pt_{doped}–$MoAl_{1-x}B$, $Pt_{ads.}$–$MoAl_{1-x}B$ (with the formation $Pt_{ads.}$–Mo interactions), and $Pt_{ads.}$–O–$MoAl_{1-x}B$ (with the formation $Pt_{ads.}$–O interactions).

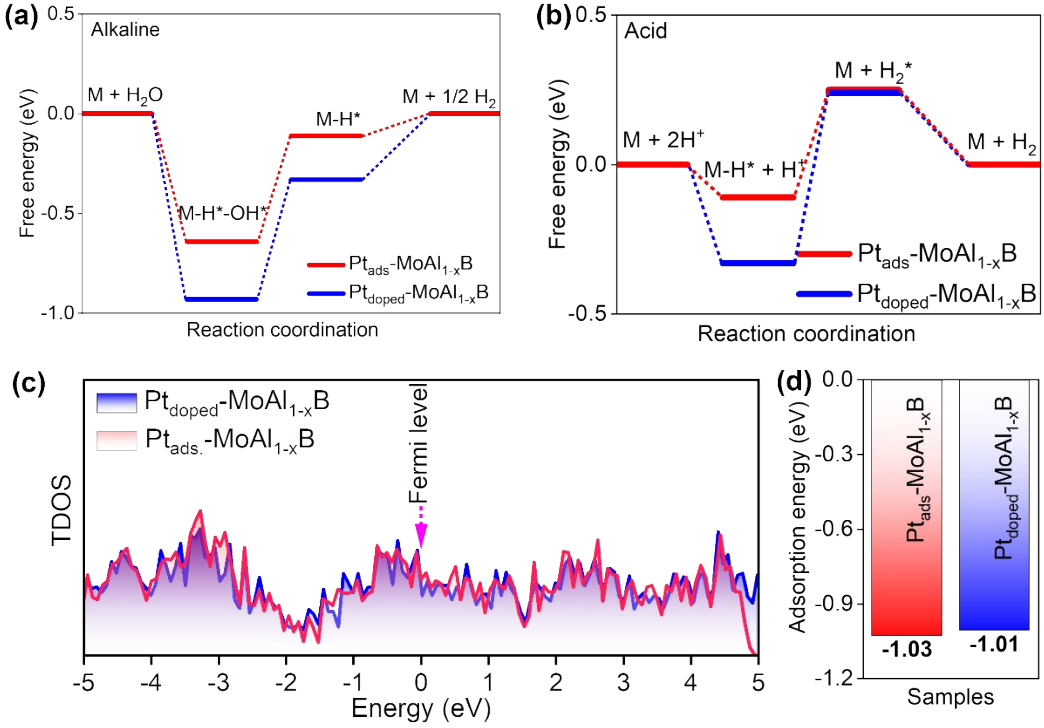

Figure S13. Gibbs free energy diagrams of Pt_{doped}–$MoAl_{1-x}B$ and $Pt_{ads.}$–$MoAl_{1-x}B$ for HER in (a) alkaline and (b) acid medium; (c) DOS and (d) water adsorption energy of Pt_{doped}–$MoAl_{1-x}B$ and $Pt_{ads.}$–$MoAl_{1-x}B$.

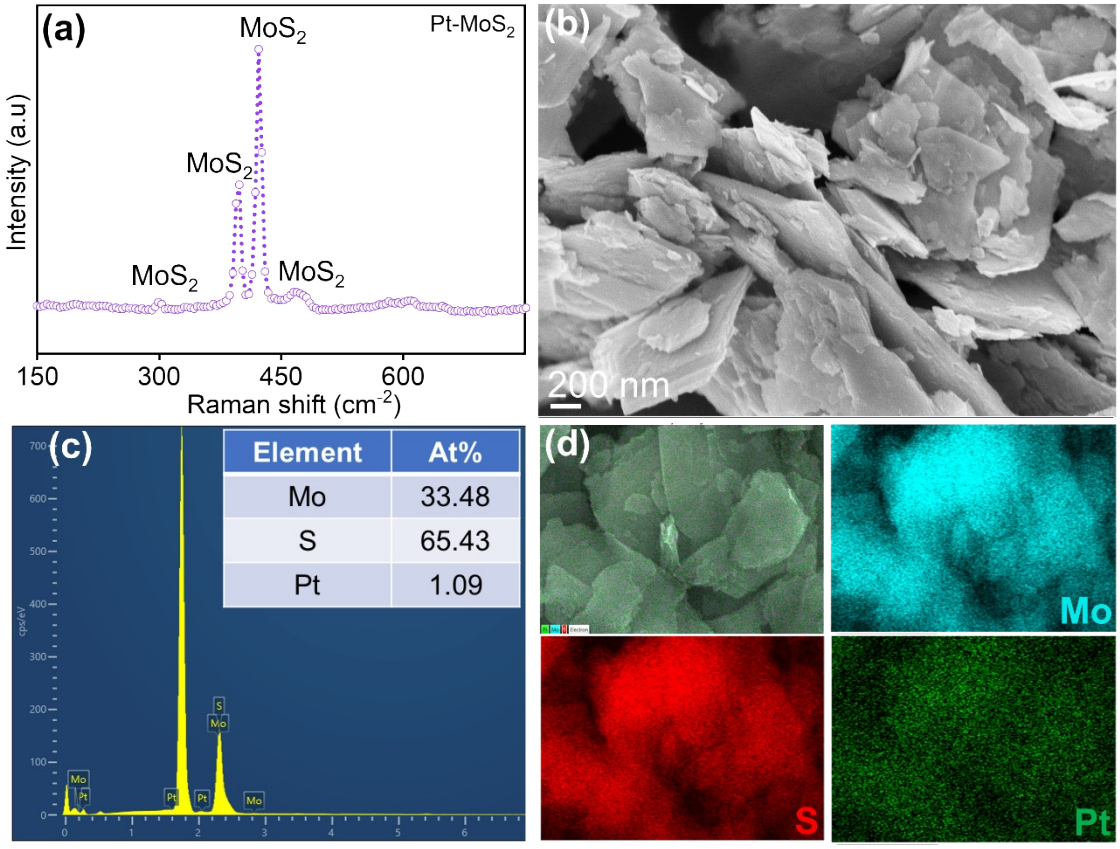

Figure S14. (a) Raman spectrum, (b) SEM image, and (c) EDS spectrum, and EDS mapping of Pt–MoS_2 material.

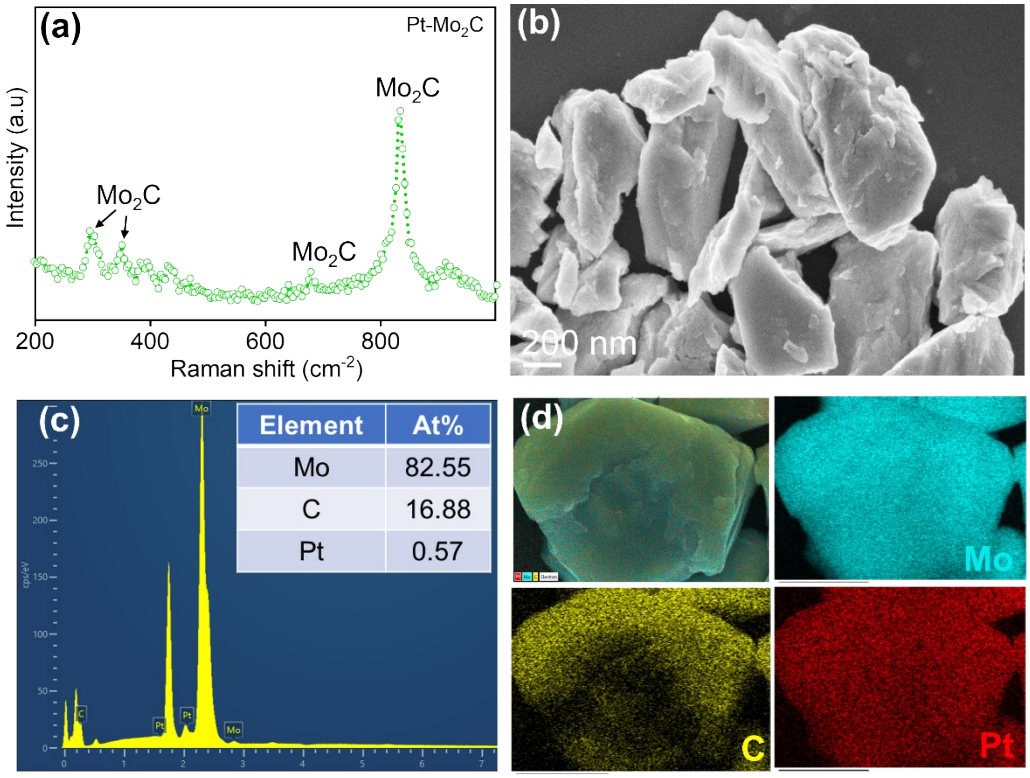

Figure S15. (a) Raman spectrum, (b) SEM image, and (c) EDS spectrum, and EDS mapping of Pt–Mo_2C material.

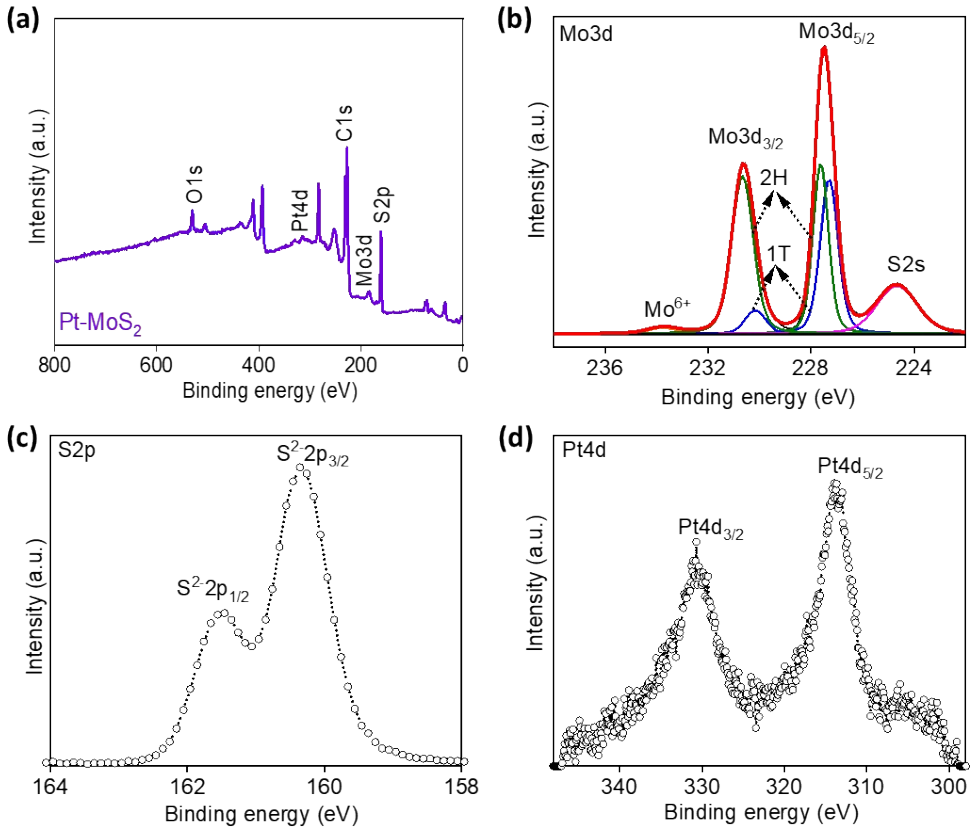

Figure S16. (a) XPS survey of Pt–MoS_2 material; High-resolution XPS spectra of (b) Mo3d, (c) S2p, and (d) Pt4d for Pt–MoS_2 material.

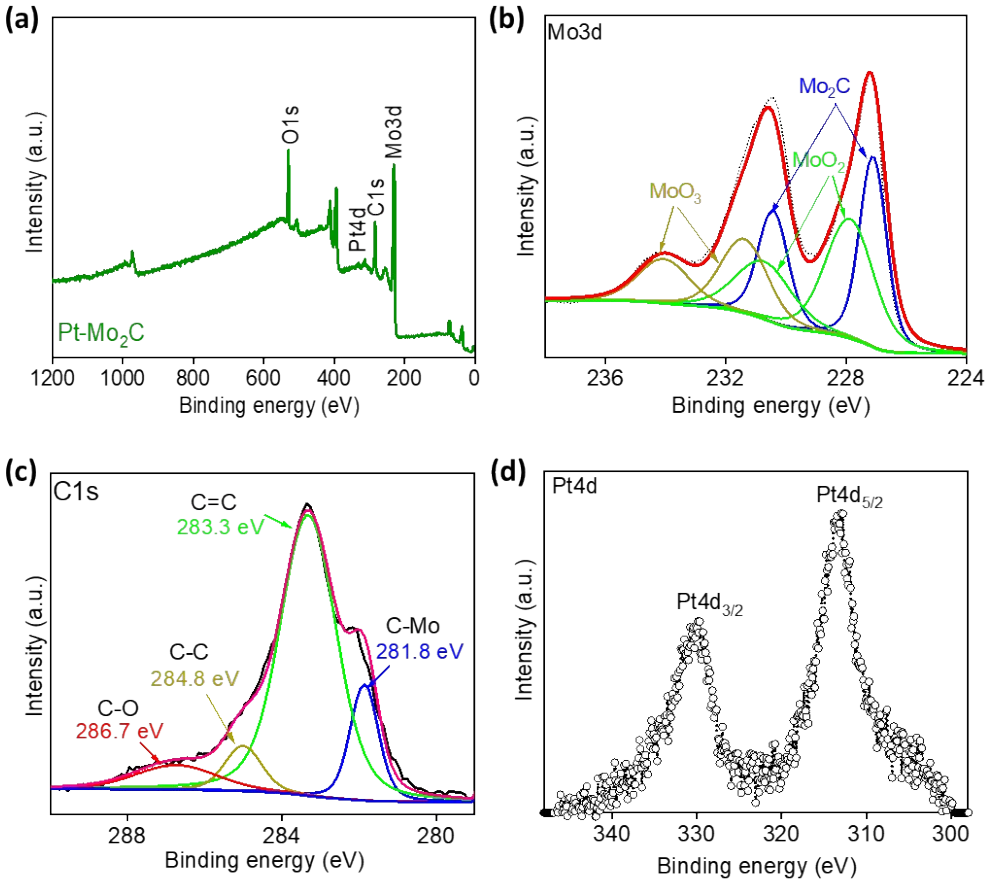

Figure S17. (a) XPS survey of Pt–Mo_2C material; High-resolution XPS spectra of (b) Mo3d, (c) C1s, and (d) Pt4d for Pt–Mo_2C material.

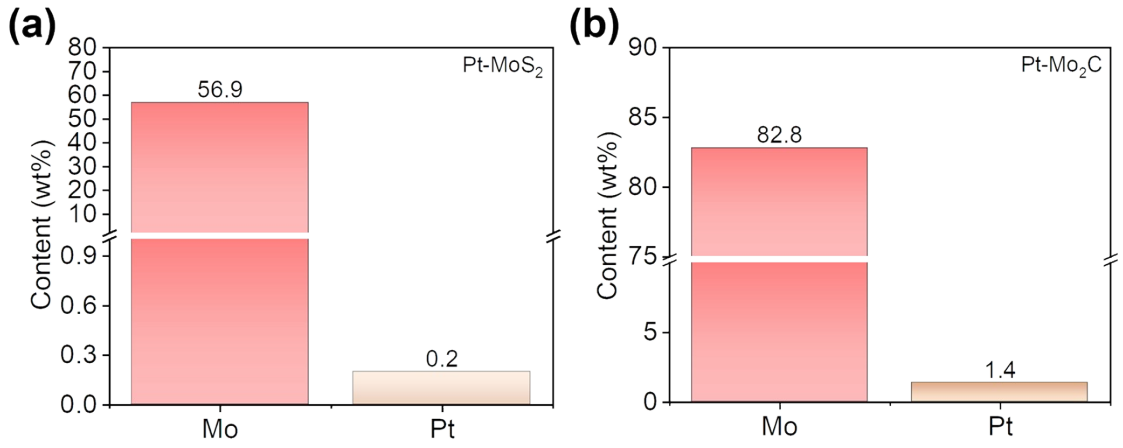

Figure S18. ICP–OES analysis for Pt content in (a) Pt–MoS_2 and (b) Pt–Mo_2C catalysts.

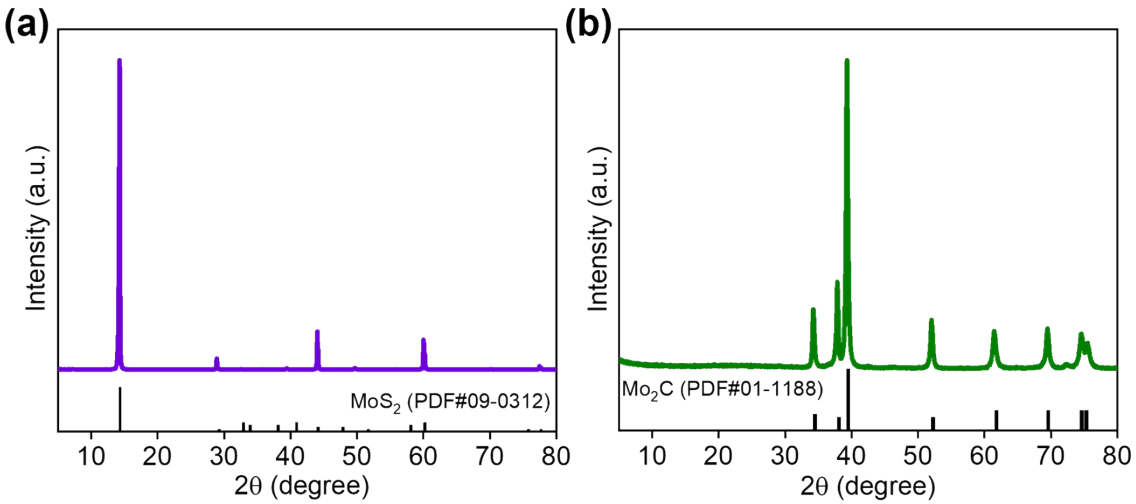

Figure S19. XRD patterns of (a) Pt–MoS_2 and (b) Pt–Mo_2C catalysts.

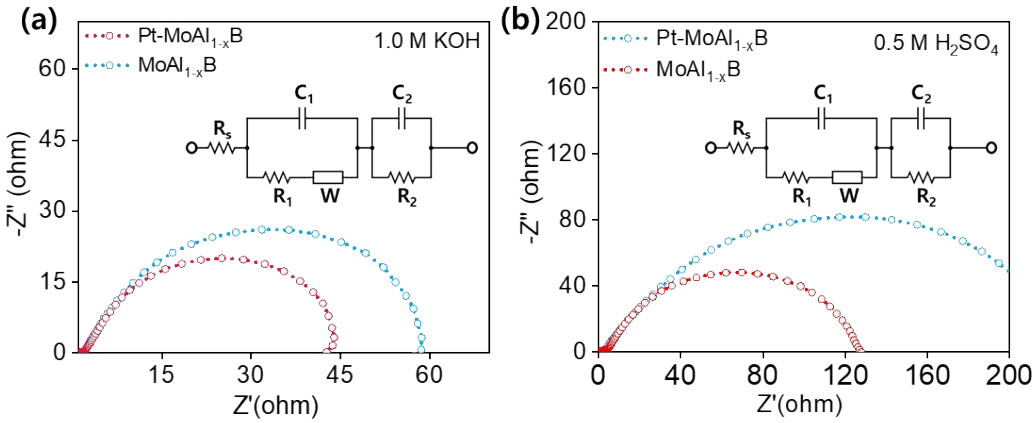

Figure S20. EIS measurements of $MoAl_{1-x}B$ and Pt–$MoAl_{1-x}B$ in (a) 1.0 M KOH and (b) 0.5 M H_2SO_4 medium at their OCP (Table S1).

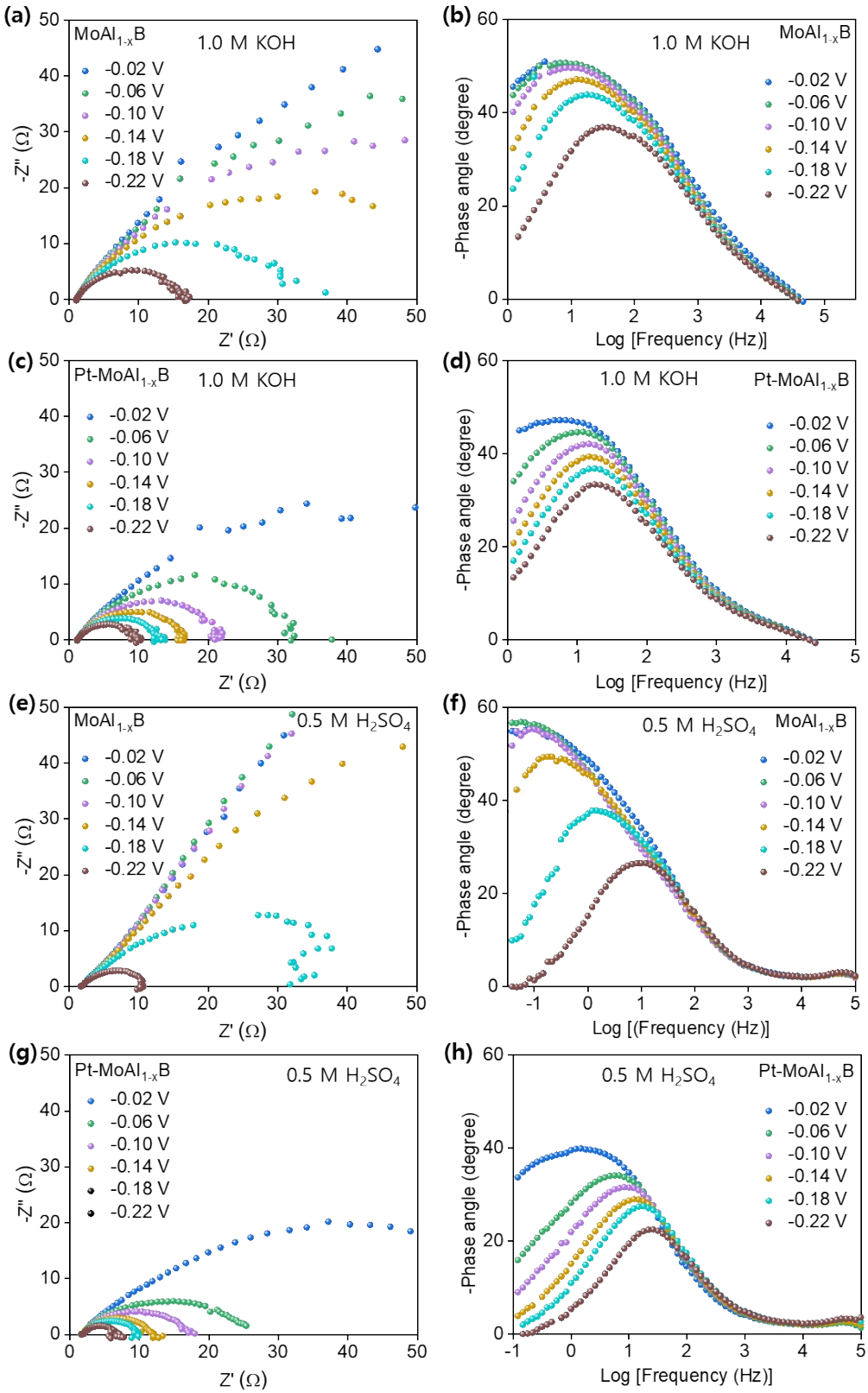

Figure S21. (a, c, e, g) Nyquist plots and (b, d, f, h) Bode plots of $MoAl_{1-x}B$ and Pt–$MoAl_{1-x}B$ at different applied potentials in 1.0 M KOH and 0.5 M H_2SO_4 medium.

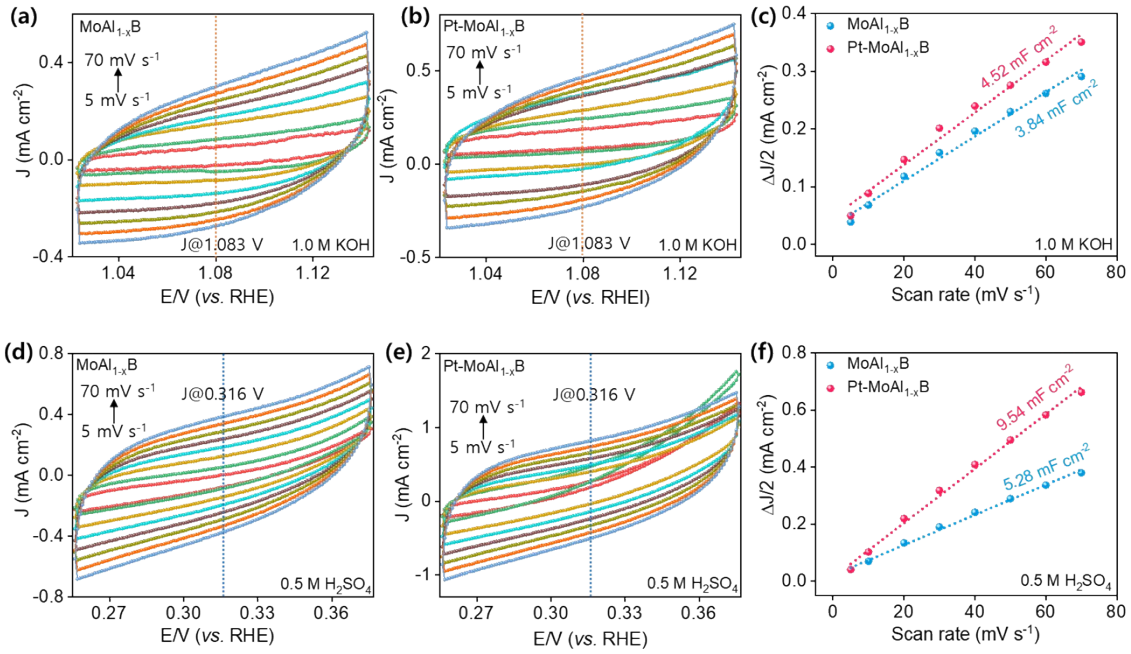

Figure S22. CV measurements of (a) $MoAl_{1-x}B$ and (b) Pt–$MoAl_{1-x}B$ at different scan rates (5, 10, 20, 30, 40, 50, 60, and 70 mV s^{-1}) in 1.0 M KOH and (c) their corresponding C_{dl} values derived from slope of ($\Delta J/2$) versus Scan rate (J value is obtained at E = 1.083 V); CV measurements of (d) $MoAl_{1-x}B$ and (e) Pt–$MoAl_{1-x}B$ at different scan rates (5, 10, 20, 30, 40, 50, 60, and 70 mV s^{-1}) in 0.5 M H_2SO_4 and (f) their corresponding C_{dl} values derived from slope of ($\Delta J/2$) versus Scan rate (J value is obtained at E = 0.316 V).

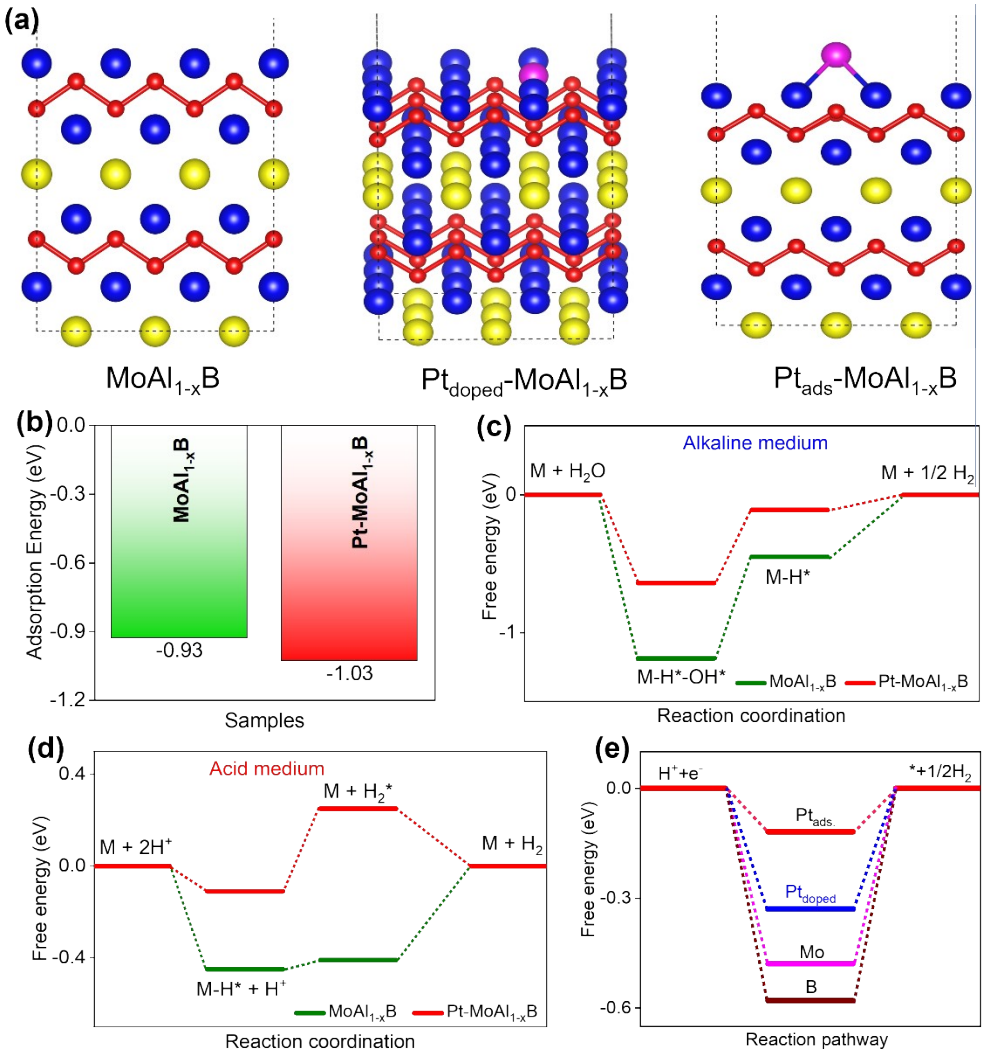

Figure S23. (a) Structural models of $MoAl_{1-x}B$ and Pt–$MoAl_{1-x}B$ materials; (b) Water adsorption energy and (c and d) ΔG diagrams of $MoAl_{1-x}B$ and Pt–$MoAl_{1-x}B$ materials for HER; (e) The ΔG_{H^*} of different active sites in Pt–$MoAl_{1-x}B$ structure for HER.

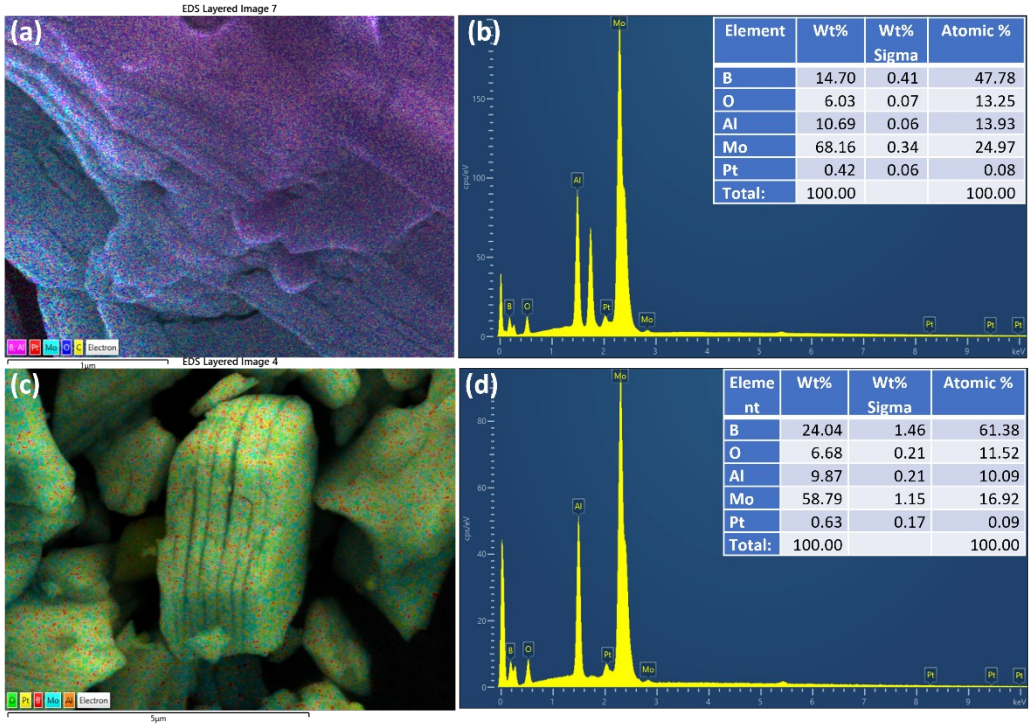

Figure S24. SEM-EDS results of Pt–$MoAl_{1-x}B$ achieved from (a and b) 200 µL and (c and d) 400 µL of initial $[PtCl_6]^{2-}$ ion precursor (10 mg mL^{-1}).

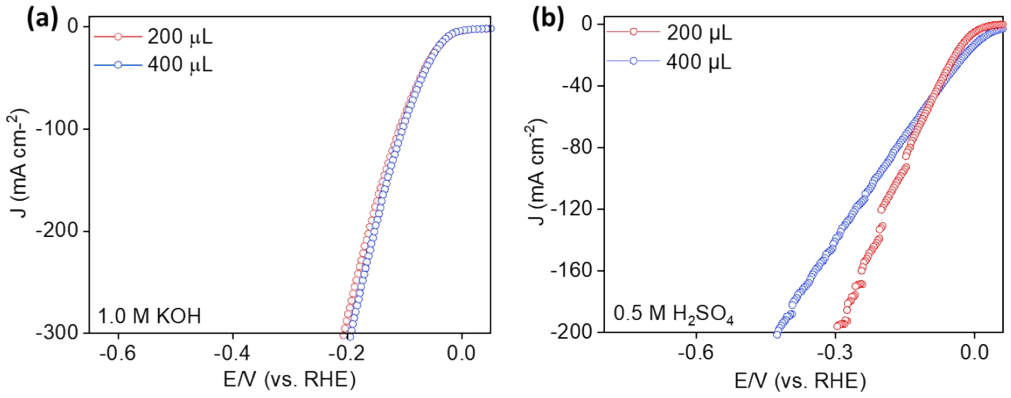

Figure S25. HER performance of Pt–$MoAl_{1-x}B$ catalyst achieved from 200 µL and 400 µL of initial $[PtCl_6]^{2-}$ ion precursor (10 mg mL^{-1}) in (a) alkaline and (b) acid media.

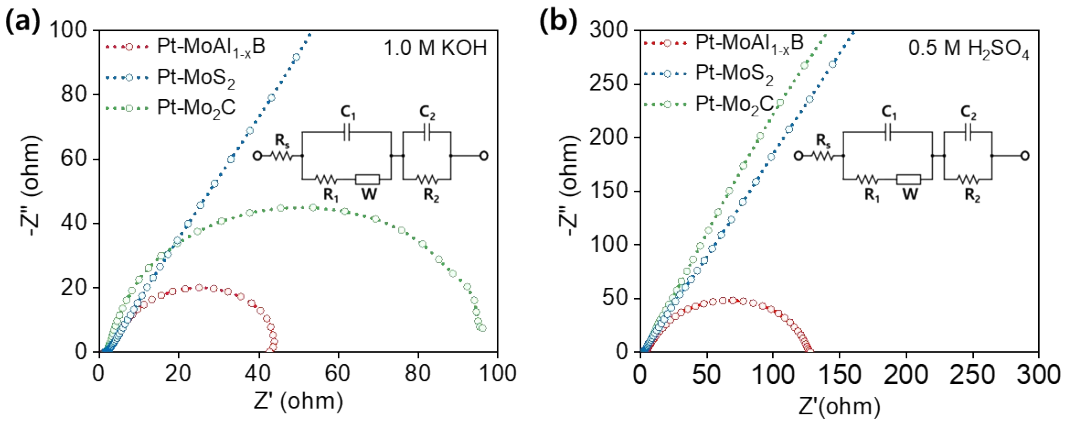

Figure S26. EIS measurements of Pt–$MoAl_{1-x}B$, Pt–Mo_2C, and Pt–MoS_2 in (a) 1.0 M KOH and (b) 0.5 M H_2SO_4 medium at their OCP (Table S1).

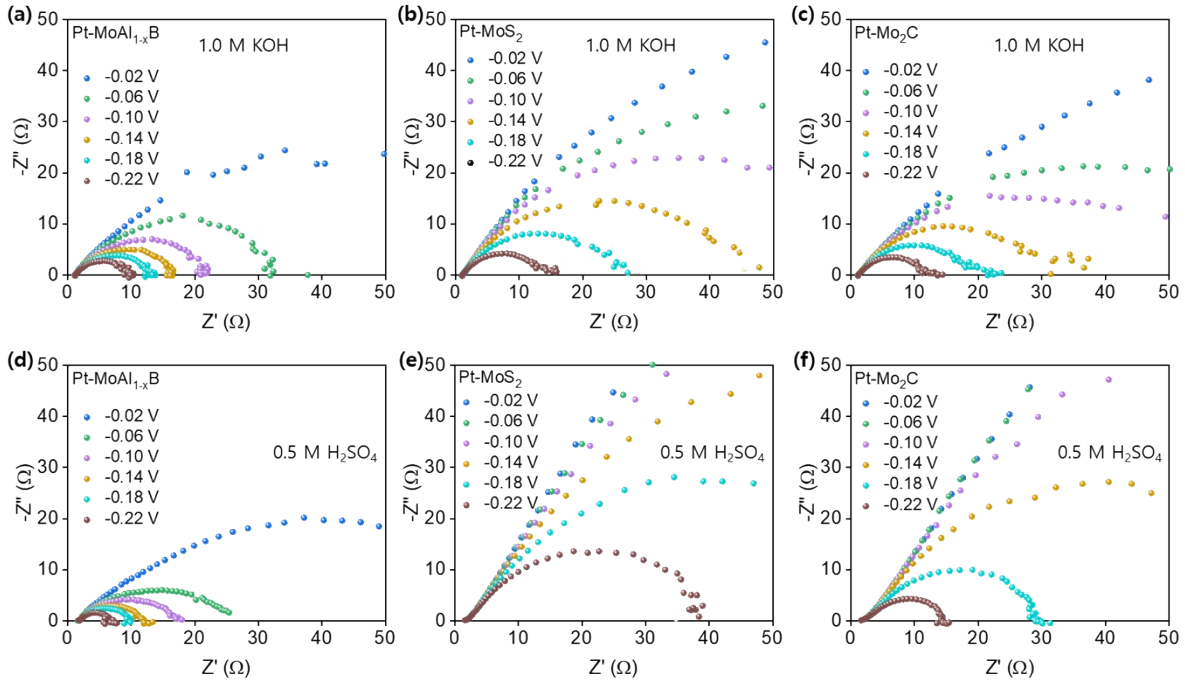

Figure S27. Nyquist plots of Pt-MoS_2, Pt-Mo_2C, and Pt–$MoAl_{1-x}B$ at different applied potential in (a-c) 1.0 M KOH and (d-f) 0.5 M H_2SO_4 medium.

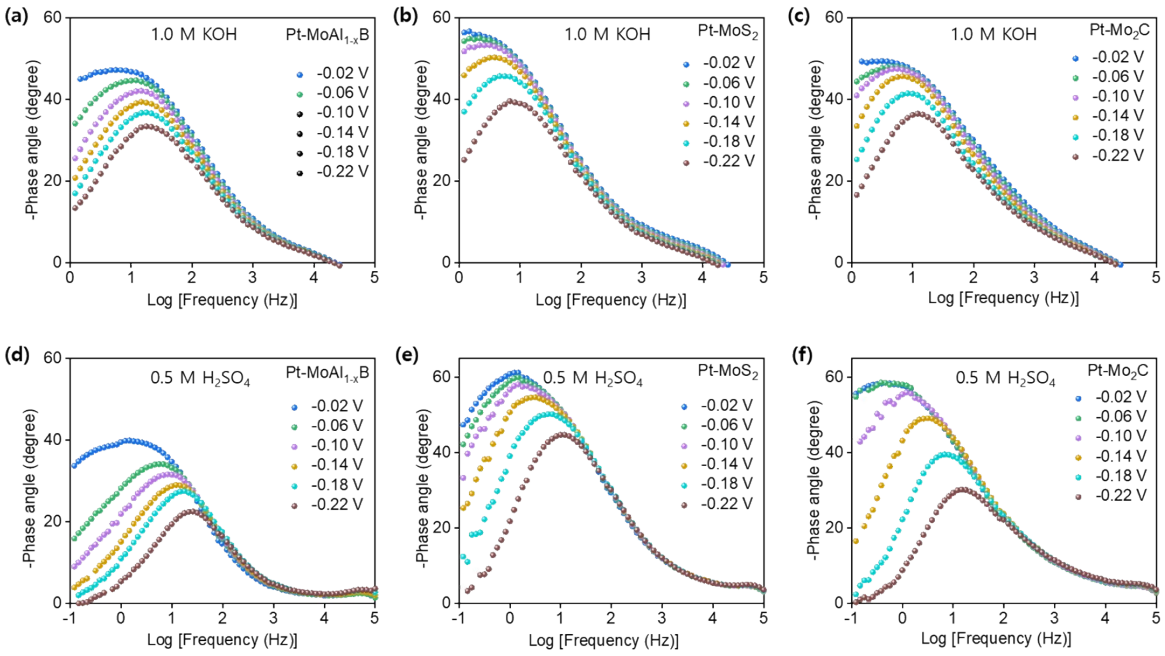

Figure S28. Bode plots of Pt-MoS_2, Pt-Mo_2C, and Pt–$MoAl_{1-x}B$ at different applied potential in (a-c) 1.0 M KOH and (d-f) 0.5 M H_2SO_4 medium.

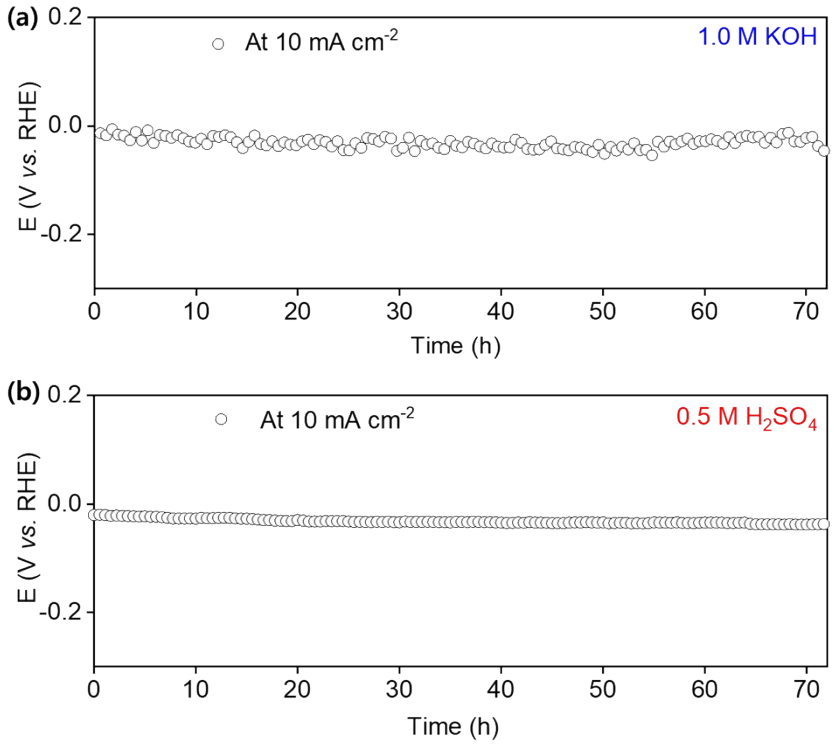

Figure S29. HER stability tests of the Pt–$MoAl_{1-x}B$ at 10 mA cm^{-2} in (a) 1.0 M KOH and (b) 0.5 M H_2SO_4 medium.

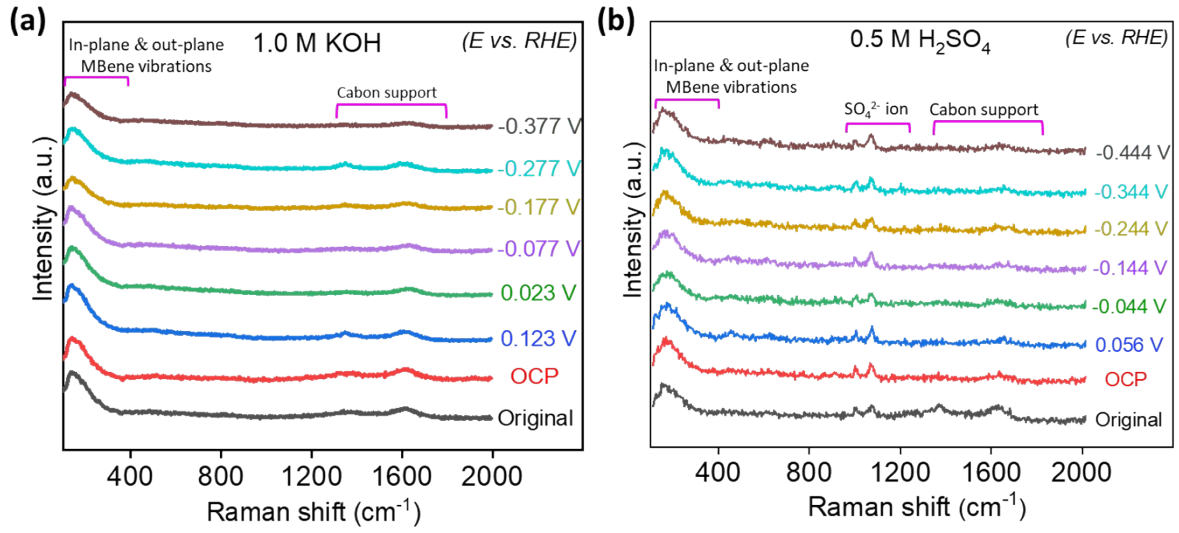

Figure S30. In situ Raman analysis of Pt–$MoAl_{1-x}B$ catalyst-based electrode during HER at different applied potentials in (a) alkaline and (b) acid media.

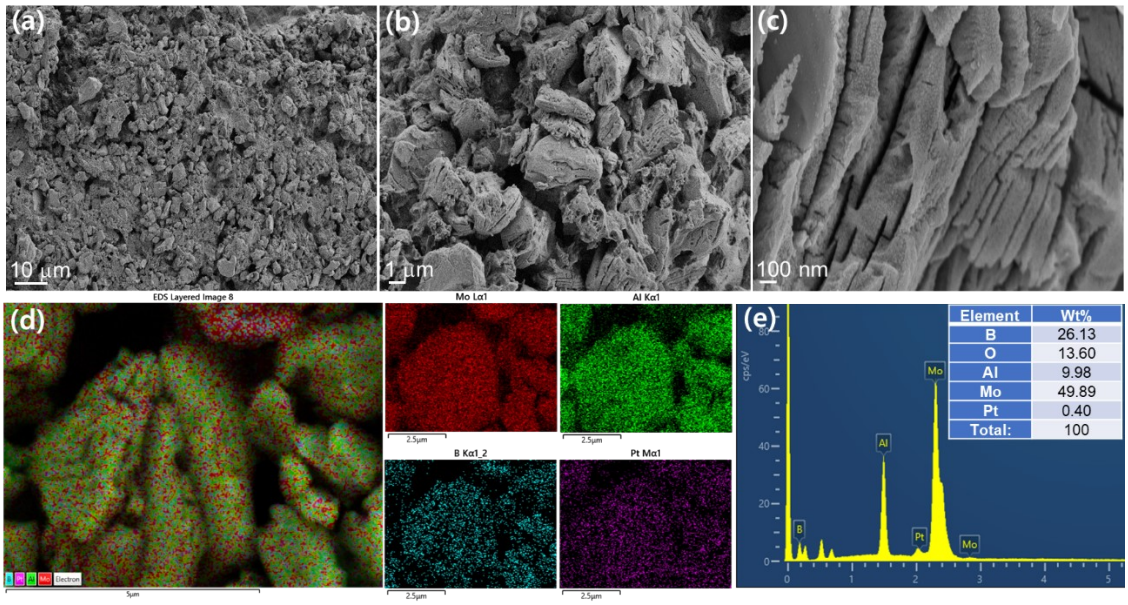

Figure S31. The morphology and structure of the post-HER Pt–$MoAl_{1-x}B$ catalyst in alkaline medium: (a-c) SEM images at different magnifications; (d) EDS color mapping image; and (e) EDS spectrum.

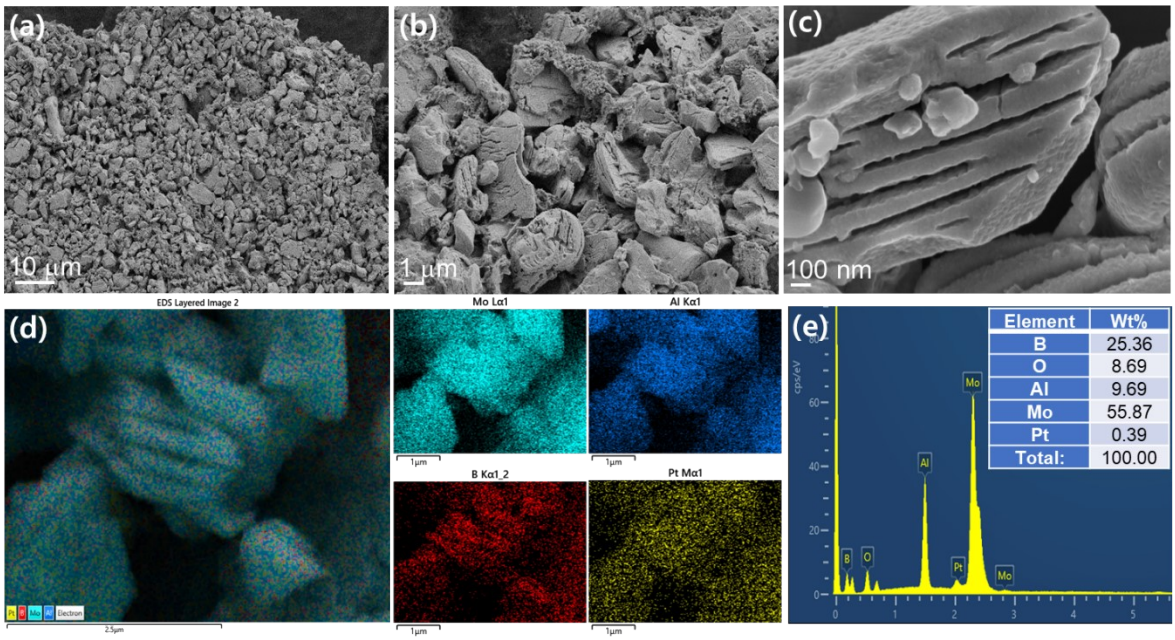

Figure S32. The morphology and structure of the post-HER Pt–$MoAl_{1-x}B$ catalyst in acid medium: (a-c) SEM images at different magnifications; (d) EDS color mapping image; and (e) EDS spectrum.

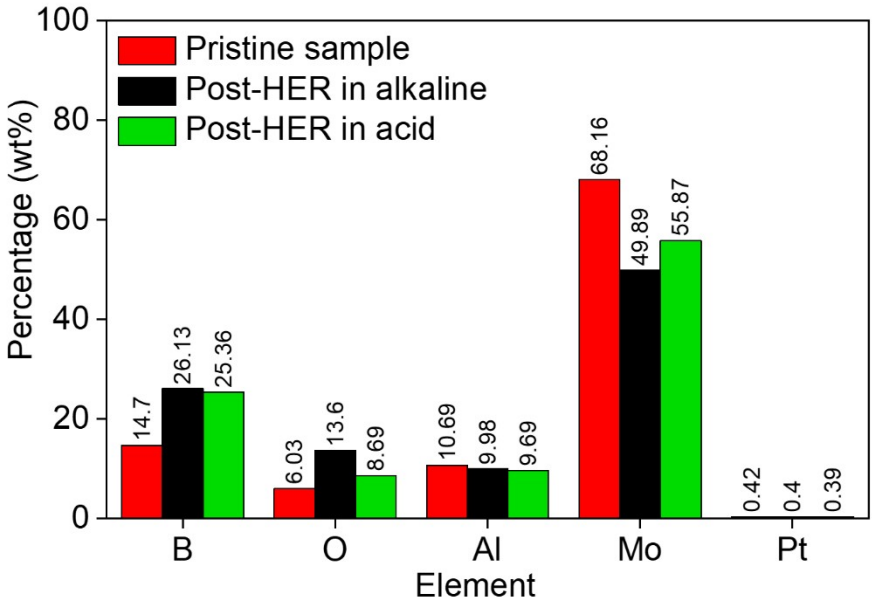

Figure S33. Comparision of element composition between pristine Pt–$MoAl_{1-x}B$ and the post-HER samples in alkaline and acid media.

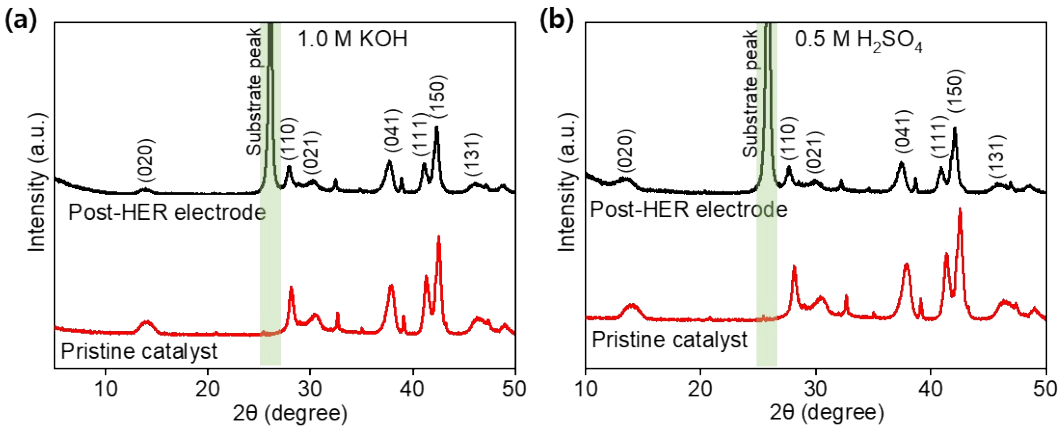

Figure S34. XRD analysis for the pristine Pt–$MoAl_{1-x}B$ catalyst and the post-HER Pt–$MoAl_{1-x}B$ based electrodes working in (a) alkaline and (b) acid medium.

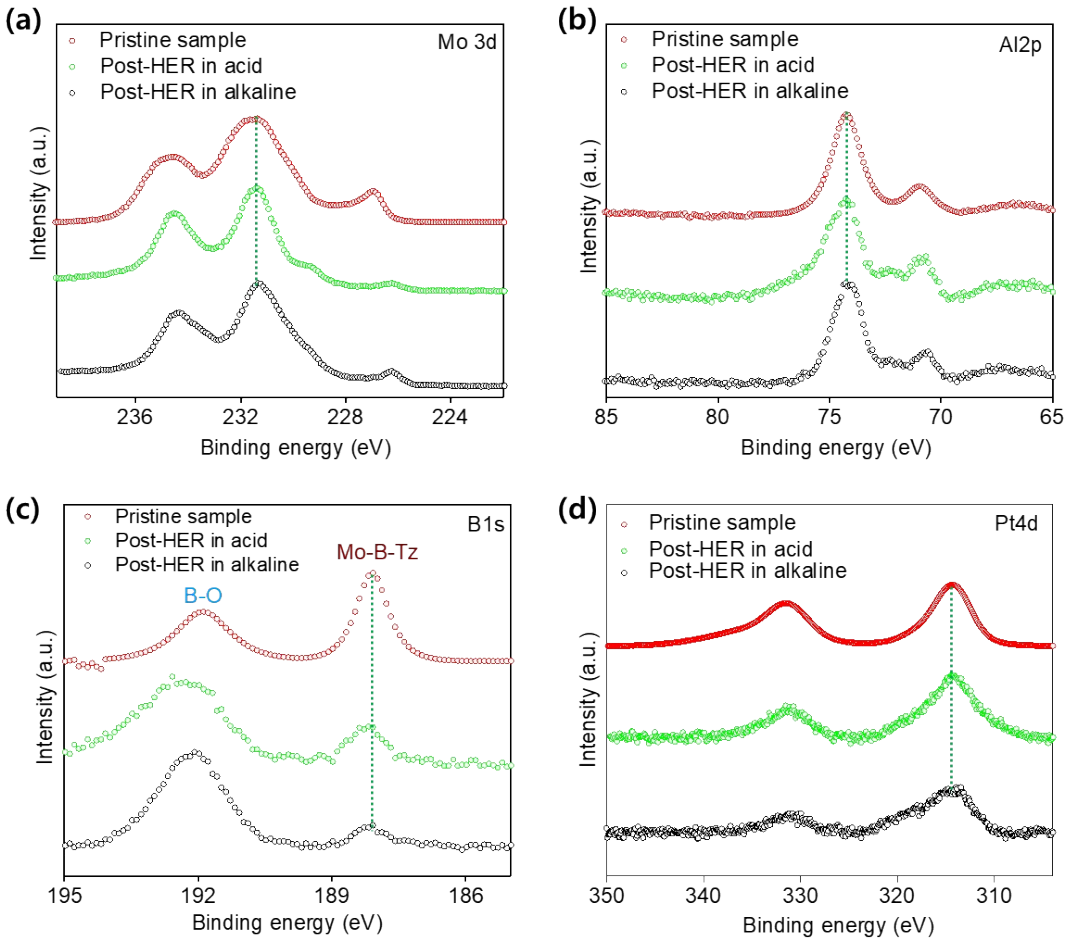

Figure S35. Comparision of element composition between pristine Pt–$MoAl_{1-x}B$ and the post-HER samples in alkaline and acid media.

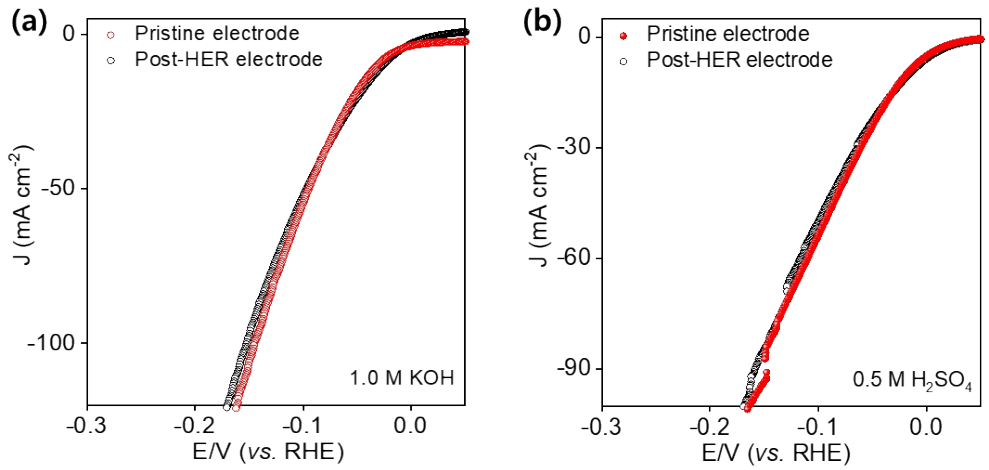

Figure S36. The LSV response of the Pt–$MoAl_{1-x}B$ based electrode before and after HER stability test in (a) alkaline and (b) acid medium at a scan rate of 5 mV s^{-1}.

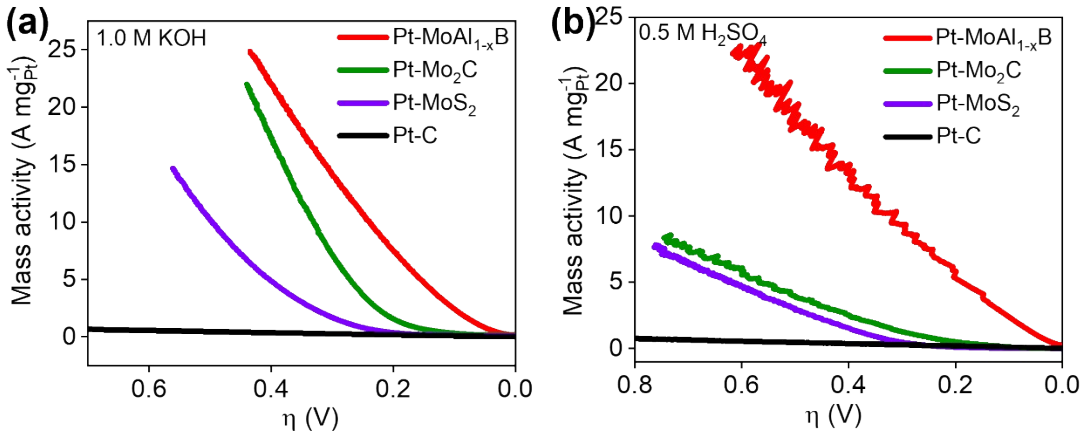

Figure S37. Mass activities of the Pt–$MoAl_{1-x}B$, Pt–Mo_2C, Pt–MoS_2, and Pt–C in (a) alkaline and (b) acid medium.

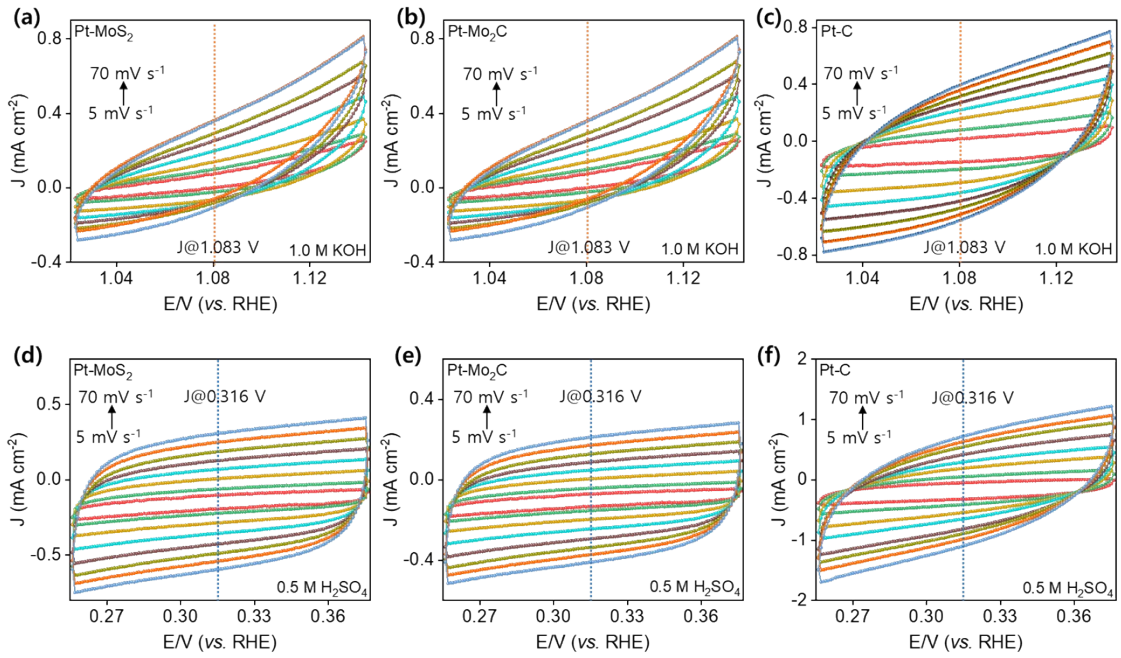

Figure S38. CV measurements of the Pt–Mo_2C, Pt–MoS_2, and Pt–C at different scan rates (5, 10, 20, 30, 40, 50, 60, and 70 mV s^{-1}) in (a-c) alkaline and (d-f) acid medium.

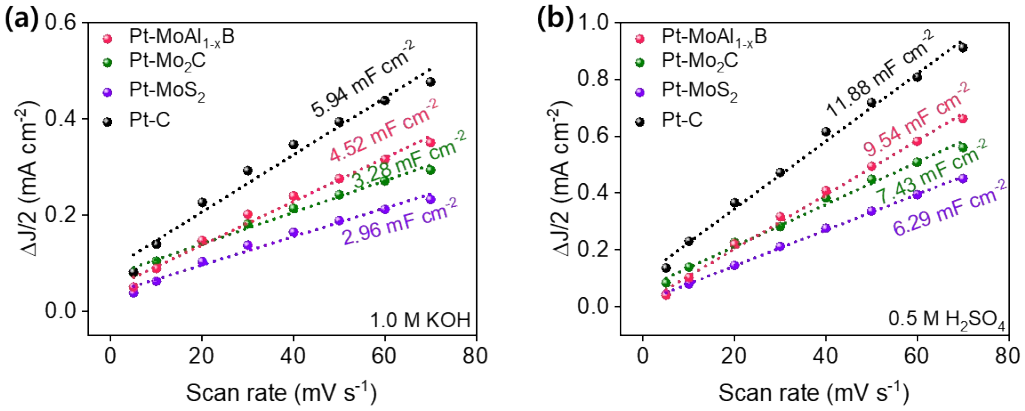

Figure S39. (a) C_{dl} value of Pt–$MoAl_{1-x}B$, Pt–Mo_2C, Pt–MoS_2, and Pt–C in alkaline derived from slope of (ΔJ/2) versus Scan rate (J value is obtained at E = 1.083 V); (b) C_{dl} value of Pt–$MoAl_{1-x}B$, Pt–Mo_2C, Pt–MoS_2, and Pt–C in acid medium derived from slope of (ΔJ/2) versus Scan rate (J value is obtained at E = 0.316 V).

The ECSA is examined by CV at various scan rates in non-faradic regions for the electrodes of catalyst-deposited NF (or CC) and bare NF (or CC) to achieve their C_{dl} values. The ECSA value are calculated by using the following equation:

$$ECSA = \frac{C_{dl}}{C_{dl(substrate)}} \qquad (4)$$

While the C_{dl} of bare NF in 1.0 M KOH is chosen as 1.56 mF cm^{-2} ,which is measured by our previous research for the same type of NF substrate,[9] the C_{dl} of bare CC in 0.5 M H_2SO_4 is found to be 0.2 mF cm^{-2} by CV measurment in Fig. S30.

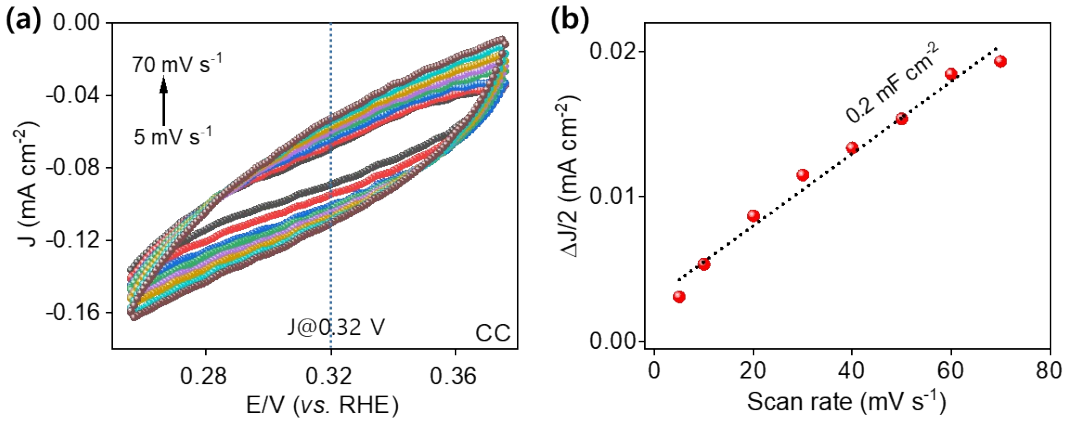

Figure S40. (a) CV measurement and (b) C_{dl} value of bare CC substrate in acid medium derived from slope of (ΔJ/2) versus Scan rate (J value is obtained at E = 0.32 V).

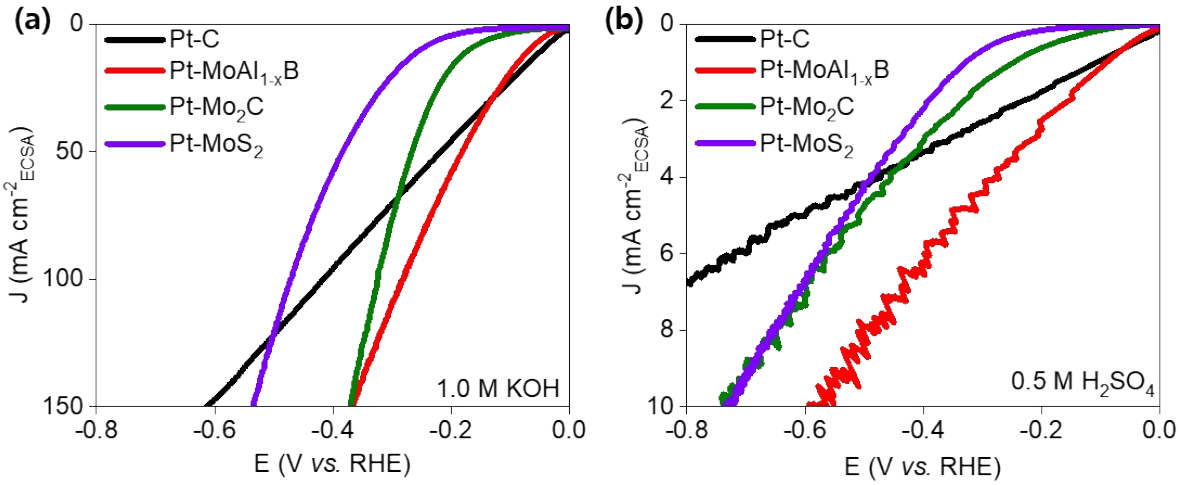

Figure S41. Specific activities of the Pt–$MoAl_{1-x}B$, Pt–Mo_2C, Pt–MoS_2, and Pt–C in (a) alkaline and (b) acid media.

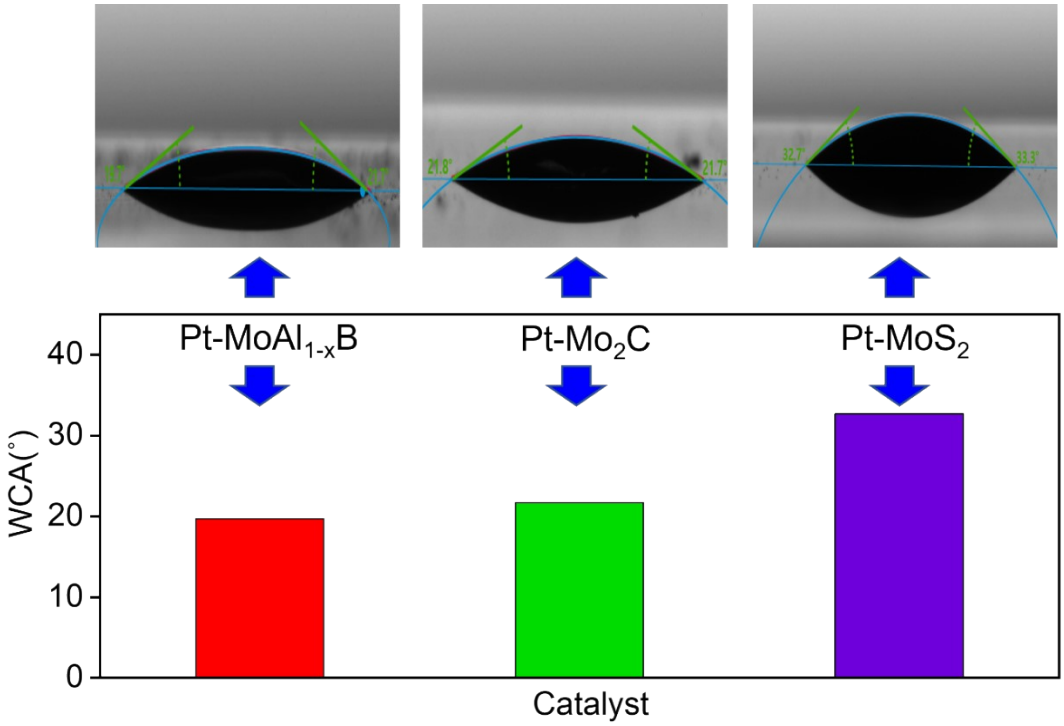

Figure S42. Water contact angle (WCA) measurement of the Pt–$MoAl_{1-x}B$, Pt–Mo_2C, and Pt–MoS_2 catalysts.

The turnover frequency (TOF) was calculated by the following equation:

$$TOF = \frac{J}{n \times m \times F} \quad (5)$$

where J is the measured geometric current density from LSV curve, n is number of active sites (mol), m is the factor (1/m implies that m electrodes are required to form one H_2 molecule from water, in other words, m value for HER is 2) and F is the Faraday constant. Note that the number of active sites (n) was assessed by cyclic voltammetry tests (Figure S33) in phosphate-buffered saline solution (1.0 M PBS, pH ~ 7), as indicated in previous reports.[9,10]

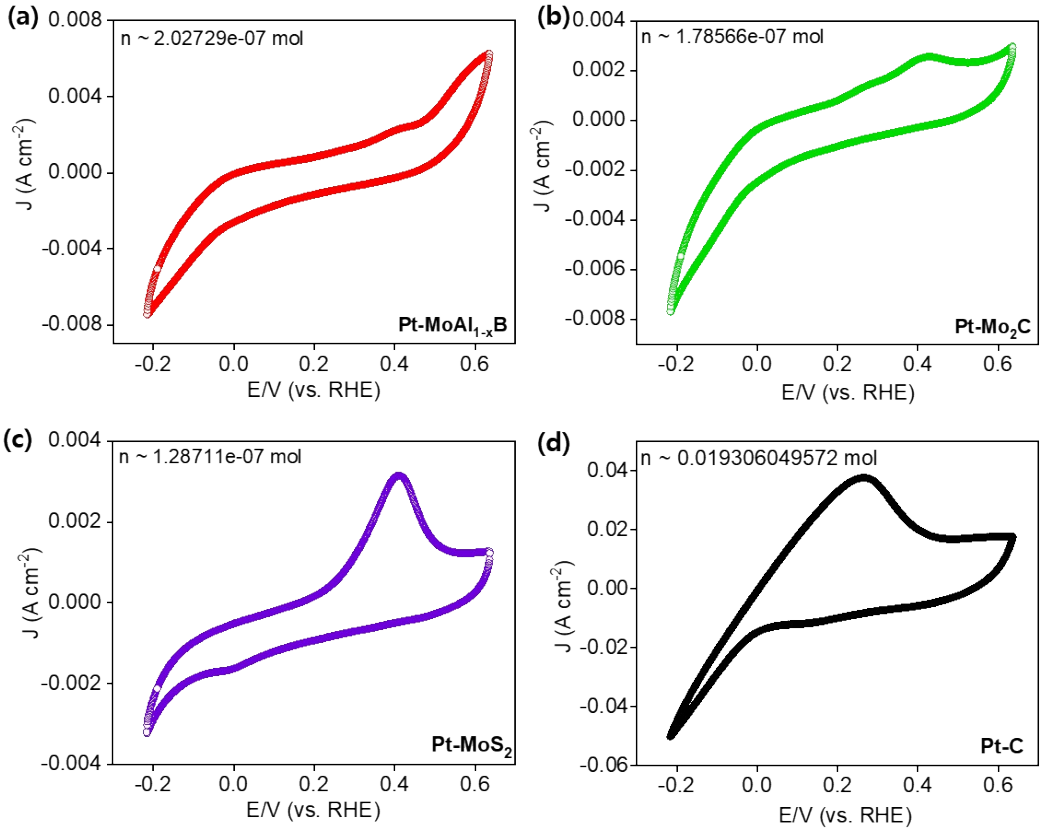

Figure S43. CV measurements of (a) Pt–$MoAl_{1-x}B$, (b) Pt–Mo_2C, (c) Pt–MoS_2, and (d) Pt-C catalysts at a scan rate of 50 mV s^{-1} in 1.0 M PBS electrolyte.

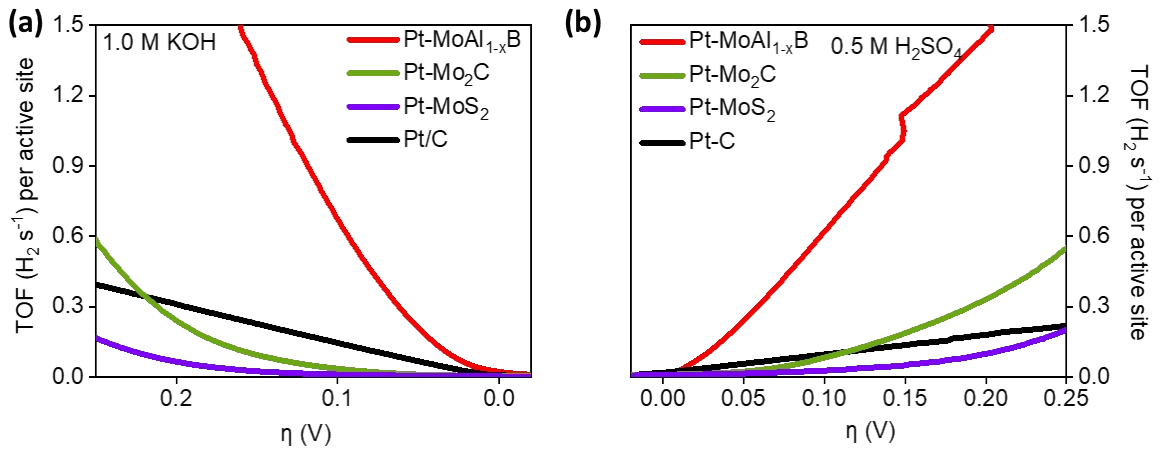

Figure 44. TOF performance of different catalysts towards HER in (a) alkaline and (b) acid media (The TOF calculation is based on the capacitance of the bulk catalysts).

We try to quantify the active Pt sites to get a better understanding of the activity via estimation of the number of active Pt sites in Pt-$MoAl_{1-x}B$, Pt-MoS_2, and Pt-Mo_2C from Pt content and Pt atomic weight (determined by ICP-OES) on the working electrode with the hypothesis that all content of Pt is single atoms and each Pt single atom accounts for one active site exposed to electrolyte. Then the TOF can be calculated as follows:

$$TOF = \frac{Total\ hydrogen\ turnovers\ per\ geometric\ area}{The\ number\ of\ active\ Pt\ centers\ per\ geometric\ area} \quad (6)$$

In which, the Total hydrogen turnovers were calculated as the following equations:

$$Total\ hydrogen\ turnovers = (|j|\ mA\ cm^{-2})\left(\frac{1\ C\ s^{-1}}{1000\ mA}\right)\left(\frac{1\ mol\ e^-}{96485\ C}\right)\left(\frac{1\ mol}{2\ mol\ e^-}\right)\left(\frac{6.022\times10^{23}\ molecules\ H_2}{1\ mol\ H_2}\right.$$
$$= 3.12\times10^{15}\ |j|\ \frac{H_2\ s^{-1}}{cm^2} per\ mA\ cm^{-2} \quad (7)$$

The number of active Pt centers were estimated from the total catalyst loading per geometric area:

$$Number\ of\ active\ Pt\ centers = \left(\frac{Catalyst\ loading\ per\ geometric\ area\ (g\ cm^{-2}) \times Pt\ content\ (wt.\%)}{Pt\ atomic\ weight\ (g\ mol^{-1})}\right) \times \left(\frac{6.022\times10^{23} atom\ Pt}{1\ mol\ Pt}\right) \quad (8)$$

Finally, the current density obtained from LSV curves can be convert into TOF value according to:

$$TOF_{Pt-MoAl1-xB} = 0.044 \times |j| \quad (9)$$

$$TOF_{Pt-Mo2C} = 0.028 \times |j| \quad (10)$$

$$TOF_{Pt-MoS2} = 0.002 \times |j| \quad (11)$$

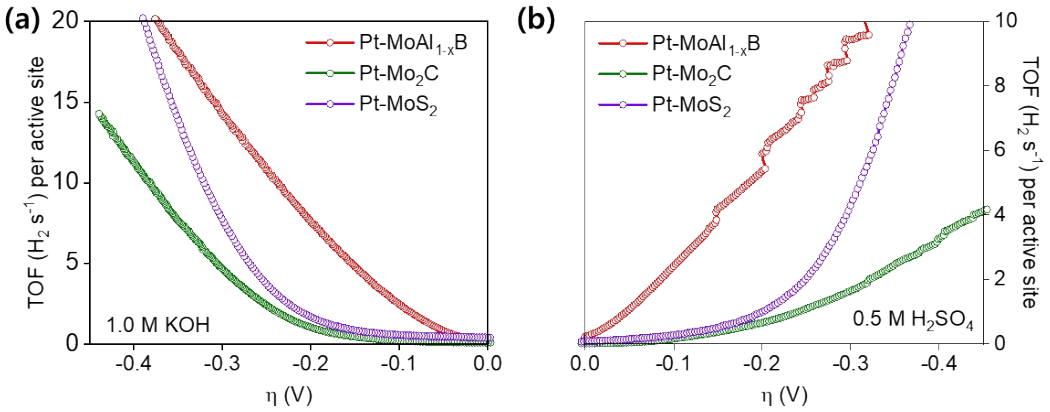

Figure S45. TOF values of Pt-$MoAl_{1-x}B$, Pt-MoS_2, and Pt-Mo_2C towards HER in (a) alkaline and (b) acid medium (The TOF calculation is based on the hypothesis that all content of Pt is single atoms and each Pt single atom accounts for one active site exposed to electrolyte).

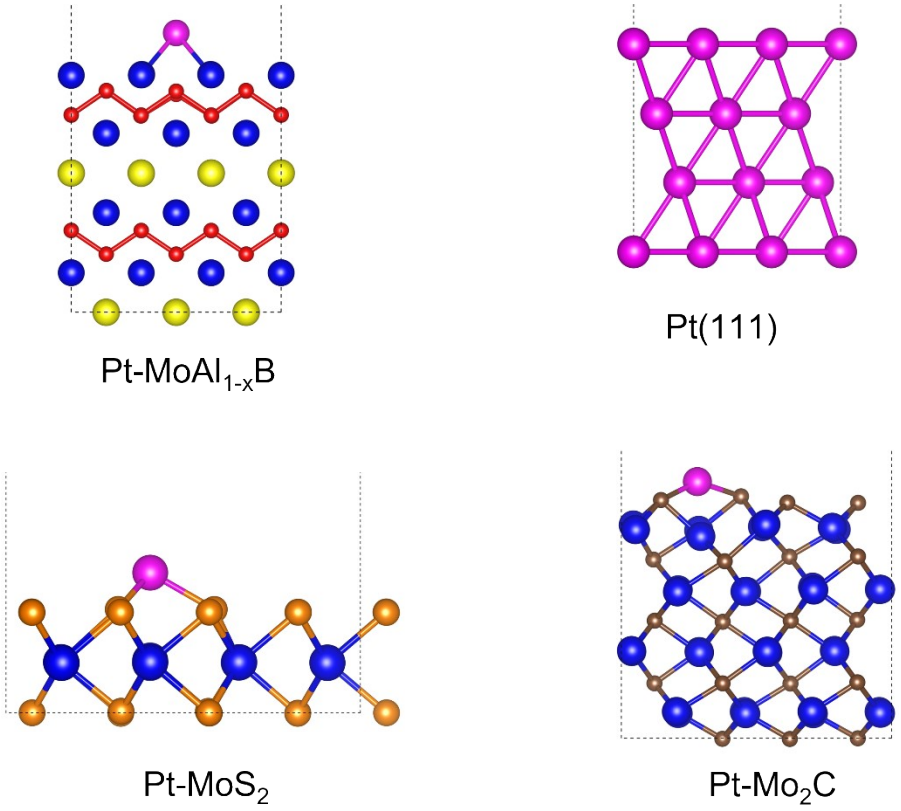

Figure S46. Theoretical material models of Pt–$MoAl_{1-x}B$, Pt–Mo_2C, Pt–MoS_2, and Pt–C for DFT calculation.

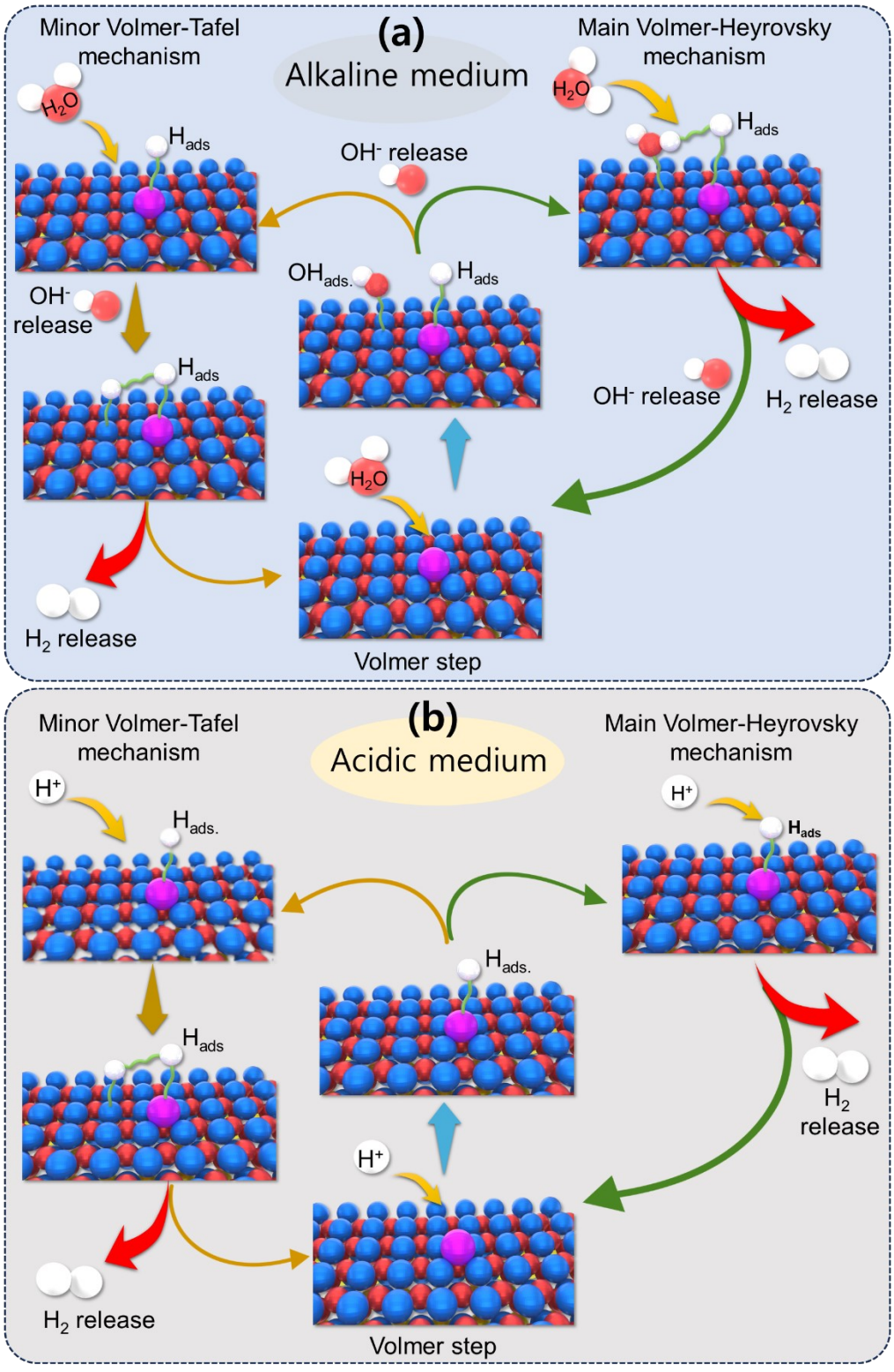

Figure S47. Schematic illustration for the main Volmer-Heyrovsky HER mechanism and minor Volmer-Heyrovsky HER mechanism occuring on Pt–$MoAl_{1-x}B$ surface in (a) alkaline and (b) acid medium.

Table S1. Open circuit potential (OCP) values of $MoAl_{1-x}B$, Pt-$MoAl_{1-x}B$, Pt-MoS_2, and Pt-Mo_2C in alkaline and acid media.

Catalysts	**OCP in 1.0 M KOH (V)**	**OCP in 0.5 M H_2SO_4 (V)**
$MoAl_{1-x}B$	-0.807	0.07
Pt-$MoAl_{1-x}B$	-0.805	0.055
Pt-Mo_2C	-0.468	0.192
Pt-MoS_2	-0.078	0.229

Table S2. Exchange current density (j_o) of $MoAl_{1-x}B$, Pt-$MoAl_{1-x}B$, Pt-MoS_2, Pt-Mo_2C, and Pt-C towards HER in alkaline and acid media.

Catalysts	**j_o in 1.0 M KOH ($mA\ cm^{-2}$)**	**j_o in 0.5 M H_2SO_4 ($mA\ cm^{-2}$)**
$MoAl_{1-x}B$	0.02	0.05
Pt-$MoAl_{1-x}B$	38.0	25.11
Pt-Mo_2C	1.69	2.81
Pt-MoS_2	0.69	0.38
Pt-C	44.6	34.67

Table S3. The ICP-OES analysis for the electrolyte after long-term stability test of Pt–$MoAl_{1-x}B$ in 1.0 M KOH medium.

Elements	Content in post-HER electrolyte (μg/mL)	Leaching content (%)
Mo	1.17	5.3
Al	0.1	2.5
B	0.04	1.6
Pt	0.0	0.0

\

Table S4. The ICP-OES analysis for the electrolyte after long-term stability test of Pt–$MoAl_{1-x}B$ in in 0.5 M H_2SO_4 medium.

Elements	Content in post-HER electrolyte (μg/mL)	Leaching content (%)
Mo	0.58	2.7
Al	0.08	2.0
B	0.03	1.2
Pt	0.0	0.0

Table S5. Comparison of η@10 mA cm^{-2} between our catalyst and recently reported representative HER catalysts in alkaline electrolyte.

Catalyst	η@10 mA cm^{-2} (mV)	References
Pt–$MoAl_{1-x}B$	32	This work
Ru/Ni-MoS_2	32	Appl. Catal. B: Environ. 298 (2021) 120557
CC@WO_3/Ru SAs	34	Chem. Eng. J. 430 (2022) 132953
Pt SA-PNPM	36	ACS Nano 16 (2022) 4116
Pt/NiRu-OH	38	Appl. Catal. B: Environ. 269 (2020) 118824
Ru-MoS_2/CC	41	Appl. Catal. B: Environ. 249 (2019) 91
IrNi-N-C	45	Nano Energy 98 (2022) 107296
PtSA-C_1N_1	46	Nat. Commun. 11 (2020) 1029
Pt_1/N-C	46	Nat. Commun. 11 (2020) 1029
Ru_1CoP/CDs	51	Angew. Chem. Int. Ed. 60 (2021) 7234
Ru@2H-MoS_2	51	Appl. Catal. B: Environ. 298 (2021) 120490
Ni_5P_4-Ru	54	Adv. Mater. 32 (2020) 1906972
Ru SAs–Ni_2P	57	Nano Energy 80 (2021) 105467
Ir_{SA}-NS-$Ti_3C_2T_x$	57.7	J. Mater. Chem. A 10 (2022) 9878
E-Co SAs	59	Adv. Funct. Mater. 31 (2021) 2100547
W_1Mo_1-NG	67	Sci. Adv. 6 (2020) eaba6586
Co-MoS_2/V_2C@CC	70.1	Chem. Eng. J. 450 (2022) 138157
SA-Ru-MoS_2	76	Small methods. 3 (2019) 1900653
Ni-1T MoS_2	91	Small 18 (2022) 2107238
Ni-SA/NC	102	Adv. Mater. 33 (2021) 2003846
Ni_1/g-CN	120	Appl. Catal. B: Environ. 264 (2020) 118521
SA-Pt/MoS_2	123	Small 18 (2022) 2104824
Cu@MoS_2	131	Appl. Catal. B: Environ. 251 (2019) 87
Co doped β-Mo_2C	141	Adv. Funct. Mater. 30 (2020) 2000561
SACo-N/C	178	Sci. Bulletin 64 (2019) 1095

Table S6. Comparison of η@10 $mAcm^{-2}$ between our catalyst and recently reported representative HER catalysts in acidic electrolyte.

Catalyst	η@10 mA cm^{-2} (mV)	References
Pt–$MoAl_{1-x}B$	18	This work
Pt-SA/α-MoO_x	19	Nano Energy 70 (2020) 104529
Pt_1/N-C	19	Nat. Commun. 11 (2020) 1029
Pt-PVP/TNR@GC	21	Angew. Chem. Int. Ed. 132 (2020) 16036
Pt-SAs/WS_2	32	Nat. Commun. 12 (2021) 3021
Pt/MXene	34	Adv. Funct. Mater. 32 (2022) 2110910
Pt SA-PNPM	35	ACS Nano 16 (2022) 4116
PtSA/OLC	38	Nat. Energy 4 (2019) 512
$Ti_3C_2T_x$-PtSA	38	Nano Lett. 22 (2022) 1398
Pt1/NMHCS	40	Adv. Mater. 33 (2021) 2008599
er-WS_2-Pt	40	Adv. Mater. 30 (2017) 1704779
Pt-MWCNTs	44	Nano Energy 63 (2019) 1038.
Ru-CoP/CDs	51	Angew. Chem. Int. Ed. 60 (2021) 7234
PtSA/S-C	53	Nat. Commun. 10 (2019) 4977.
Pt-MoS_2	60	Energy Environ. Sci. 8 (2015) 1594
MXene@Pt/SWCNTs	62	Adv. Funct. Mater. 30 (2020) 2000693
CM@Ru	63	Adv. Energy. Mater. 10 (2020) 2000882
CNT–V–Fe–Ru	64	ACS Catal. 13 (2023) 49
PtN_x/TiO_2	67	Nano Energy 73 (2020) 104739
RuSA-N-S-$Ti_3C_2T_x$	76	Adv. Mater. 31 (2019) 1903841
Pt-decorated VS_2	77	ACS Nano 14 (2020) 5600
Rh/SiNW	85	Nat. Commun. 7 (2016) 12272
Pt@PCM	105	Sci. Adv. 4 (2018) 6657
Pt@PM	106	Sci. Adv. 4 (2018) eaao6657
Co-MoS_2	137	Angew. Chem. Int. Ed. 133 (2021) 7327

Table S7. Comparison of TOF@η = 100 mV between our catalyst and recently reported representative HER catalysts in alkaline electrolyte.

Catalyst	TOF@η = 100 mV (s^{-1})	References
Pt–$MoAl_{1-x}B$	0.68	This work
NiP_2-CeO_2	0.593	Inorg. Chem. 57 (2018) 548
Co-NiS_2	0.55	Angew. Chem. Int. Ed. 58 (2019) 18676
RuNP@RuN_x-OFC/NC	0.49	Appl. Catal. B: Environ. 307 (2022) 121193
$MoNi_4/MoO_2$@Ni	0.4	Nat. Commun. 8 (2017) 15437
Ru/NG-750	0.35	ACS Appl. Mater. Interfaces 9 (2017) 3785
Ru/g-C_3N_4-C-TiO_2	0.28	ACS Appl. Mater. Interfaces 13 (2021) 46608
Cu/BP	0.275	Nature Commun. 13 (2022) 5496
Ru@GnP	0.26	Adv. Mater. 30 (2018) 1803676
Pt@CoS	0.131	Appl. Catal. B: Environ. 315 (2022) 121534
Ni-MoS_2	0.08	Energy & Environ. Sci. 9 (2016) 2789
Ru-MoS_2/CC	0.062	Appl. Catal. B: Environ. 249 (2019) 91

Table S8. Comparison of TOF@η = 100 mV between our catalyst and recently reported representative HER catalysts in acidic electrolyte.

Catalyst	TOF@η = 100 mV (s^{-1})	References
Pt–$MoAl_{1-x}B$	0.627	This work
CoN_x/C	0.41	PNAS 115 (2018) 12692
CoN_x/C	0.39	Nat. Commun. 6 (2015) 7992
Co-NG-MW	0.385	Adv. Mater. 30 (2018) 1802146
Co-NC	0.36	Nano Res. 15 (2022) 3913
Ru@GnP	0.26	Adv. Mater. 30 (2018) 1803676
$Mo_{1-x}V_xSe_2$	0.25	ACS Nano 15 (2021) 14672
Ni-Mo_2C/GNS	~0.24	J. Catal. 388 (2020) 122
MoS_2/Ni_2O_3H	0.14	Small 16 (2020) 2002212
MoP|S	0.12	Small Methods 6 (2022) 2200295
Ni_2P	0.064	Energy Environ. Sci. 8 (2015) 1027
CoP NPs	0.046	Angew. Chem. Int. Ed. 53 (2014) 5427

Table S9. Comparison of performance between our developed AEMWE single cell and recent reports.

Catalyst	Cell voltage (V)	Current density (A cm^{-2})	Electrolyte and temprature	References
Pt–$MoAl_{1-x}B_{(-)}$//$RuO_{2(+)}$	1.85	0.5	1.0 M KOH and 60 °C	This work
Pt–$MoAl_{1-x}B_{(-)}$//$RuO_{2(+)}$	2.0	1.0	1.0 M KOH and 60 °C	This work
Ni/(CeO_2-La_2O_3)/$C_{(-)}$//$CuCoO_{x(+)}$	1.9	0.47	1% K_2CO_3 and 43 °C	Angew. Chem. Int. Ed. 53 (2014) 1378
Ni/(CeO_2–La_2O_3)/$C_{(-)}$//$CuCoO_{x(+)}$	1.95	0.5	1% K_2CO_3 and 60 °C	Int. J. Hydrogen Energy, 42 (2017) 10752
NiCoO-NiCo/$C_{(-)}$//CuCoO	1.85	0.504	1.0 M KOH and 50 °C	Appl Catal B Environ. 292 (2021) 120170
Co_3S_4 NS/$NF_{(-)}$//$Cu_{0·81}Co_{2·19}O_{4(+)}$	2.0	0.431	1.0 M KOH and 45–48 °C	Int. J. Hydrogen Energy 45 (2020) 36
Pt/KB 40%$_{(-)}$//$NiMn_2O_{4(+)}$	2.0	0.53	1.0 M KOH and 80 °C	Int. J. Hydrogen Energy 45 (2020) 9285
Platinum black$_{(-)}$//$NiCoFeO_{x(+)}$	2.29 2.492	0.5 1	1.0 M KOH and 50 °C	ACS Catal. 9 (2019) 7
Ag nanoparticle$_{(-)}$//NiFeCr-$LDH_{(+)}$	2.11	1	1.0 M KOH and 40 °C	Small 18 (2022) 2200303
Pt/$C_{(-)}$//$CoSb_2O_{6(+)}$	1.9	0.8	1.0 M KOH and 60 °C	ACS Energy Lett. 6 (2021) 364
Pt/$C_{(-)}$//NiCoFe–$NDA_{(+)}$	1.8 2.0	0.325 ~0.55	1.0 M KOH and 50 °C	Energy Environ. Sci. 14 (2021) 6546
Raney $Ni_{(-)}$//NiFe LDH/$NiS_{(+)}$ Ni foam$_{(-)}$//NiFe LDH/$NiS_{(+)}$	2.01 2.27	0.4 1	30% KOH and 80–85°C	Adv. Energy Mater. 11 (2021) 2102353
Ni-Co-S/$CP_{(-)}$//IrO_2/$CP_{(+)}$	2.4	1.7	1.0 M KOH	Int. J. Energy

			and 50 °C	Res. 45 (2021) 1918
Cu–Co–P/$CP_{(-)}$//IrO_2/$CP_{(+)}$	1.9	0.7	1.0 M KOH and 50 °C	Int. J. Hydrog. Energy 46 (2021) 19789
NiMo/Nickel $felt_{(-)}$//NiFe/Nickel $felt_{(+)}$	1.91	0.6	1.0 M KOH and 80 °C	J. Membrane Sci. 633 (2021) 119418
Pt $mesh_{(-)}$//S-$FeOOH_{+1000}$/$IF_{(+)}$	2.12	1	1.0 M KOH and 25 °C	Appl. Catal. B: Environ. 315 (2022) 121571
MoO_2/$Ni_{(-)}$//Ni $foam_{(+)}$	2.0	0.55	1.0 M KOH and 60 °C	J. Mater. Chem. A 11 (2023) 5789
$NiFe_2O_4$/stainless-steel fiber $paper_{(-)}$//NiFeCO/Ni fiber $paper_{(+)}$	2.2	0.88	1.0 M KOH and 50 °C	J. Mater. Chem. A 10 (2022) 8401

References

1. Park, Y. S. *et al.* Commercial anion exchange membrane water electrolyzer stack through non-precious metal electrocatalysts. *Appl Catal B* **292**, 120170 (2021).
2. King, L. A. *et al.* A non-precious metal hydrogen catalyst in a commercial polymer electrolyte membrane electrolyser. *Nat Nanotechnol* **14**, 1071–1074 (2019).
3. Kresse, G. & Furthmüller, J. Efficiency of ab-initio total energy calculations for metals and semiconductors using a plane-wave basis set. *Comput Mater Sci* **6**, 15–50 (1996).
4. Kresse, G. & Furthmüller, J. Efficient iterative schemes for ab initio total-energy calculations using a plane-wave basis set. *Phys Rev B* **54**, 11169–11186 (1996).
5. Kresse, G. & Joubert, D. From ultrasoft pseudopotentials to the projector augmented-wave method. *Phys Rev B* **59**, 1758–1775 (1999).
6. Perdew, J. P. *et al.* Generalized Gradient Approximation Made Simple. *Phys Rev Lett* **77**, 3865–3868 (1996).
7. Wang, V. *et al.* VASPKIT: A user-friendly interface facilitating high-throughput computing and analysis using VASP code. *Comput Phys Commun* **267**, 108033 (2021).
8. Grimme, S., Antony, J., Ehrlich, S. & Krieg, H. A consistent and accurate ab initio parametrization of density functional dispersion correction (DFT-D) for the 94 elements H-Pu. *J Chem Phys* **132**, 154104 (2010).
9. Nguyen, T. H. *et al.* Metal Single-Site Molecular Complex–MXene Heteroelectrocatalysts Interspersed Graphene Nanonetwork for Efficient Dual-Task of Water Splitting and Metal–Air Batteries. *Adv Funct Mater* **33**, 2210101 (2023).
10. Chang, K. *et al.* A 3D hierarchical network derived from 2D Fe-doped NiSe nanosheets/carbon nanotubes with enhanced OER performance for overall water splitting. *J Mater Chem A* **10**, 3102–3111 (2022).